Received: 12 October 2020 | Accepted: 27 March 2021

DOI: 10.1002/stc.2756

RESEARCH ARTICLE

WILEY

Enhanced motion control performance of the tuned mass damper inerter through primary structure shaping

Zixiao Wang | **Agathoklis Giaralis**

Department of Civil Engineering, City, University of London, London, UK

Correspondence
Agathoklis Giaralis, Department of Civil Engineering, City, University of London, London, UK.
Email: agathoklis@city.ac.uk

Summary

The tuned mass damper inerter (TMDI) is a linear passive dynamic vibration absorber widely considered in the literature to mitigate the motion of dynamically excited primary structures. Previous studies focused on optimal TMDI tuning approaches and connectivity arrangements to improve motion control efficiency for some given primary structure. This paper investigates the influence of the elastic and mass properties of the primary structure to the TMDI motion control performance. This is pursued through an innovative parametric study involving a wide range of tapered beam-like cantilevered primary structures with different continuously varying flexural rigidity and mass distributions equipped with TMDIs optimally tuned for resonant harmonic and for white noise excitations. Optimal TMDI tuning and performance assessment are expedited through a novel simplified two-degree-of-freedom dynamic model, which accounts for the properties of the primary structure. It is found that reduced free-end displacement and TMDI stroke are achieved for primary structures in which the ratio of flexural rigidity over mass decreases faster with height resulting in vibration modal shapes with higher convexity. The latter is quantified though the average modal curvature shown to be well correlated with TMDI motion control improvement. It is concluded that judicial shaping of the primary structure extends the applicability of the TMDI to structures where connecting the inerter away from the free end is practically challenging while contains the magnitude of the inerter and damping forces exerted to the primary structure. Therefore, this study paves the way towards combining optimal TMDI tuning with primary structure design for improved performance to dynamic loads.

KEYWORDS

continuous dynamical system modeling, inerter and damping forces, mode shape curvature, optimal passive vibration control, structural system shaping, tuned mass damper inerter

1 | INTRODUCTION

Recent advances in computer-aided engineering design together with the availability of high-performance materials enable the construction of ever-more slender cantilevered civil engineering structures including high-rise buildings, industrial chimneys, and wind turbine towers. Such structures are typically lightweight and material efficient, thus promoting sustainability in construction.[1] However, they are prone to develop excessive lateral oscillations under the action of wind and earthquakes due to their low inherent damping and resonant natural frequencies, which can lead to serviceability or even structural failures.[2] To this end, supplemental damping devices and passive vibration absorbers are commonly employed to safeguard the resilience of flexible cantilevered structures to wind and seismic loads.[3] In this context, the tuned mass damper (TMD) has been widely used in practice for lateral vibrations suppression of flexible cantilevered structures including tall buildings,[4,5] industrial chimneys,[6] and solar towers,[7] as well as heavily investigated for motion control of wind turbine towers.[8,9] The typical TMD consists of a free-to-oscillate secondary mass attached to the top of the cantilevered structure via linear stiffeners/springs and viscous damper (dashpot) elements.[10] For a given secondary mass, the TMD stiffness and damping properties are "tuned" to the fundamental (dominant) vibration mode of the uncontrolled (or primary) structure such that significant kinetic energy is transferred from the primary structure to the oscillating secondary mass and dissipated by the damping element.[11,12] In this setting, the TMD vibration control efficacy depends on its inertia: the larger the attached TMD mass is, the more effective and robust to detuning effects the TMD becomes.[13] However, practical constraints limit the TMD weight that can be accommodated at the top of slender structures while TMD up-front cost increases with the attached mass.[14]

To this end, in recent years, the inertia property of the inerter, defined by Smith[15] as a linear massless mechanical element resisting relative acceleration through the inertance constant, has been leveraged to relax requirements for large secondary mass in suppressing the motion of dynamically excited civil engineering structures via passive dynamic vibration absorbers.[16–21] Among these absorbers, the TMDI, introduced by Marian and Giaralis,[22] was shown to outperform the conventional TMD for the seismic protection of fixed-based buildings[18,23–28] and base-isolated buildings,[29,30] as well as for mitigating wind-borne vibrations in buildings[31–33] and wind turbine towers.[34] In this respect, it was found that the incorporation of an inerter to the TMD can lead to significant attached mass reduction since the inertance scales up practically independently of inerter device physical mass in actual device embodiments.[15,35,36] For fixed-based buildings, this is achieved by using an inerter to connect the secondary mass attached to one building floor (commonly the top floor/roof) to a different (lower) floor. The early works of Marian and Giaralis[18,22] showed that TMDI motion control efficacy improves with increasing inertance. Later, Giaralis and Taflanidis[25,37] demonstrated significantly enhanced and robust seismic performance to uncertainties in TMDI-equipped multistorey shear frames as the inerter spans more floors (i.e. as the inerter connects the secondary mass to a more distant lower floor from the floor that the mass is attached to). This trend was confirmed in various real-life and benchmark structures under earthquake and wind excitations.[26,32,33]

More recently, Wang and Giaralis[38] showed that TMDI motion control potential in wind-excited tall buildings improves by decreasing the stiffness of the floor where the TMDI is located through a local modification of the primary structure. Furthermore, Pietrosanti et al.[39] demonstrated that the relative modal coordinate of the floor where the secondary mass is attached to and the floor where the inerter is attached to influences significantly the effectiveness of TMDI to suppress vibrations in lumped-mass models of earthquake excited buildings. In this regard, collectively, the works of Wang and Giaralis[38] and Pietrosanti et al.[39] point to the fact that the stiffness and/or mass properties of the primary structure influence the motion control efficacy of the TMDI. Nevertheless, the quantification of this influence has not been systematically pursued to date as all previous works have focused on leveraging the TMDI inertial properties (i.e., secondary mass and inertance) and inerter connectivity to mitigate the response of TMDI-equipped structures to dynamic excitations. This paper addresses the above gap in the literature through a novel parametric investigation involving a wide range of TMDI-equipped structures modeled as cantilevered continuous beams with various geometrical shapes. Numerical work is expedited by putting forth a novel simplified two-degree-of-freedom (2-DOF) model of the considered structures, which accounts for flexural rigidity and mass distribution of the primary structure as well as the modal coordinate of the primary structure at the location where the inerter connects to. The investigation is further supported by optimal TMDI tuning aiming to minimize the free-end peak and root-mean-square (RMS) displacement response of the primary structure subject to harmonic resonant and white noise excitation, respectively. Optimal TMDI tuning and performance assessment are facilitated by using analytically derived frequency response functions (FRFs) of the 2-DOF model. Attention is focused on quantifying the influence of the primary structure geometrical shape to the free-end displacement reduction, secondary mass stroke, inerter force, and damping force.

The remainder of the paper is organized as follows. In Section 2, the governing equations of motion of a TMDI-equipped cantilevered beam accommodating any inerter connecting location are established in terms of a set of nondimensional TMDI and primary structure parameters in frequency domain via treating the TMDI-controlled continuous cantilever as a 2-DOF system. A set of FRFs corresponding to response quantities of practical interest are derived analytically. Optimal TMDI design/tuning is considered in Section 3 for minimizing the steady-state displacement response of the primary structure subject to harmonic resonant and to white noise force excitation. Section 4 introduces and discusses parametric geometric shape variation of the primary structure and its influence on the fundamental mode shape, which is used in subsequent sections for investigating the effect of primary structure shaping to the motion control potential of the TMDI. The accuracy of the 2-DOF model for optimal TMDI design/tuning is verified against detailed finite element (FE) models for a wide range of TMDI parameters and primary structure shapes. Next, Section 5 furnishes and discusses comprehensive numerical results shedding light to the effectiveness of optimally designed TMDI in containing vibration of cantilevered beams with different mass and stiffness/flexibility distributions under resonant harmonic and white noise force excitations. Finally, Section 6 summarizes main conclusions.

2 | TWO-DOF MODELING AND ANALYSIS OF TMDI-EQUIPPED CONTINUOUS FLEXURAL CANTILEVER STRUCTURES

2.1 | System description and equations of motion in time domain

Consider a fixed-base structure amenable to be modeled as a continuous cantilevered beam with height h and with distributed flexural rigidity $EI(x)$ and mass per unit length $m(x)$ where $0 \le x \le h$ as depicted in Figure 1a. This generic beam model can well represent slender tall buildings, industrial chimneys, wind turbine towers, and solar towers. Further, let a TMDI be attached to the free end/tip of the considered beam (primary structure) to control the beam lateral motion due to a horizontal distributed dynamic load $p(x,t)$ as shown in Figure 1b. The TMDI comprises a secondary mass m_{TMDI} attached to the primary structure through a linear spring with stiffness k_{TMDI} in parallel with a dashpot with damping coefficient c_{TMDI}. The secondary mass is further connected to the primary structure at height χ from the ground (fixed end) through an inerter element with inertance b.

Next, assume that under the external load $p(x,t)$, the lateral response of the uncontrolled primary structure can be faithfully approximated by a single deflected time-invariant shape $\psi(x)$. Under this assumption, the response displacement of the primary structure can be written as[40]

$$u(x,t) = \psi(x) z(t), \tag{1}$$

where $z(t)$ is the free-end displacement of the cantilever and $\psi(x)$ satisfies the fixed-end boundary conditions and is normalized such that $\psi(h) = 1$ (Figure 1c). In this setting, the continuous beam can be represented by a generalized single-degree-of-freedom (SDOF) oscillator whose equation of motion is readily derived using the principle of virtual work.[40]

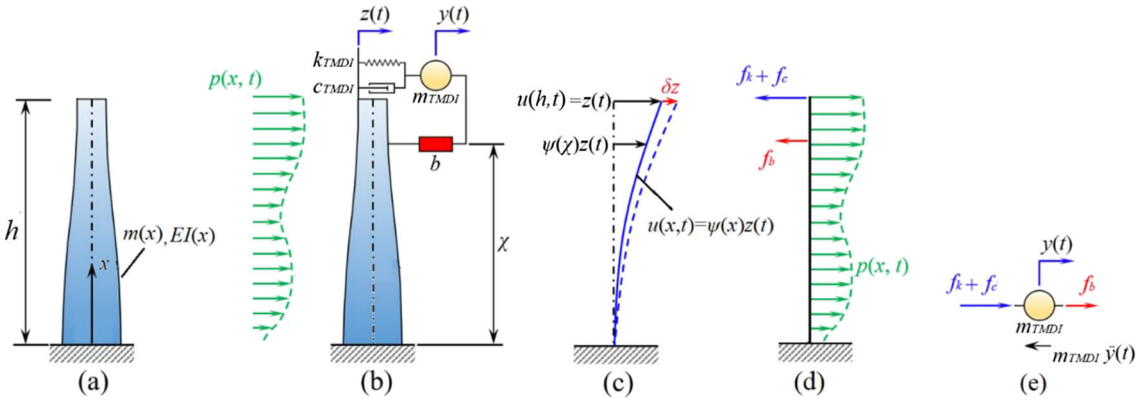

FIGURE 1 (a) Continuous flexural cantilevered uncontrolled (primary) structure, (b) TMDI-controlled structure, (c) assumed deflected shape and virtually deflected shape, (d) external loads acting on the primary structure, and (e) external loads acting on the TMDI mass

Specifically, the virtual work done by the inertial resistance and the external forces acting onto the primary structure shown in Figure 1d due to some virtual displacement δz at the free end of the primary structure is given as

$$\delta W_E = \int_0^h p\,\delta u(x)\,dx - \int_0^h f_I \delta u(x)\,dx - f_b \delta u(\chi) - (f_c + f_k)\delta u(h), \tag{2}$$

where $\delta u(x) = \psi(x)\delta z$. In the above equation, f_I is the distributed inertial resistance of the primary structure, f_b is the force of the TMDI inerter element acting at $x = \chi$ height, and f_c and f_k are the forces of the TMDI damper (dashpot) and spring elements, respectively, acting at $x = h$ (free end). These forces are given as

$$f_I = m(x)\ddot{u}(x,t), f_b = b[\psi(\chi)\ddot{z} - \ddot{y}], f_c = c_{TMDI}(\dot{z} - \dot{y}), \text{and} f_k = k_{TMDI}(z - y), \tag{3}$$

where a dot over a symbol signifies differentiation with time and $y(t)$ is the displacement of the secondary mass (Figure 1b). Further, the virtual work done by the internal flexural and damping forces of the primary structure due to the same virtual displacement δz is given as

$$\delta W_I(t) = \int_0^H EI(x)\left[\frac{\partial^2 u(x,t)}{\partial x^2} + a_c \frac{\partial^2 \dot{u}(x,t)}{\partial x^2}\right]\frac{d^2\psi}{dx^2}\delta z\,dx, \tag{4}$$

assuming that stresses due to inherent damping of the primary structure are proportional to the strain velocity by a constant a_c.

By setting $\delta W_E = \delta W_I$ and manipulating algebraically Equations (2)–(4), the following equation of motion is reached:

$$\left(m^* + b\psi(\chi)^2\right)\ddot{z} - b\psi(\chi)\ddot{y} + (c^* + c_{TMDI})\dot{z} - c_{TMDI}\dot{y} + (k^* + k_{TMDI})z - k_{TMDI}y = p^*(t), \tag{5}$$

written in terms of the free-end displacement $z(t)$ of the primary structure and the TMDI secondary mass displacement $y(t)$. In the above equation, $p^*(t)$, m^*, c^*, and k^* are the generalized load, mass, damping, and stiffness, respectively, of an underlying generalized SDOF system, which represents the primary structure in the considered simplified model. These generalized quantities are defined as

$$\begin{aligned} p^*(t) &= \int_0^h p(x,t)\psi(x)dx, \quad m^* = \int_0^h m(x)(\psi(x))^2 dx, \\ c^* &= a_c \int_0^h EI(x)\left(\frac{d^2\psi}{dx^2}\right)^2 dx = a_c k^* \quad \text{and} \quad k^* = \int_0^h EI(x)\left(\frac{d^2\psi}{dx^2}\right)^2 dx. \end{aligned} \tag{6}$$

Further to Equation (5), an additional independent equation of motion can be written in terms of the displacements $z(t)$ and $y(t)$ by taking equilibrium of the external forces acting on the secondary mass and making use of d'Alembert's principle as follows (Figure 1e):

$$\begin{aligned} &f_k + f_c + f_b = m_{TMDI}\ddot{y} \ \text{ or} \\ &b\psi(\chi)\ddot{z} - (m_{TMDI} + b)\ddot{y} + c_{TMDI}(\dot{z} - \dot{y}) + k_{TMDI}(z - y) = 0. \end{aligned} \tag{7}$$

Next, the two equations of motion, Equations (5) and (7), are rewritten as

$$\begin{cases} \left(1 + \beta\psi(\chi)^2\right)\ddot{z} - \beta\psi(\chi)\ddot{y} + 2\xi_1\omega_1\dot{z} + 2\nu\xi(\mu+\beta)\omega_1(\dot{z} - \dot{y}) + \omega_1^2 z + \nu^2\omega_1^2(\mu+\beta)(z - y) = \dfrac{p^*(t)}{m^*} \\ \beta\psi(\chi)\ddot{z} - (\mu+\beta)\ddot{y} + 2\nu\xi(\mu+\beta)\omega_1(\dot{z} - \dot{y}) + \nu^2(\mu+\beta)\omega_1^2(z - y) = 0 \end{cases} \tag{8}$$

with the aid of the circular natural frequency of the generalized SDOF primary structure representation, $\omega_1 = (k^*/m^*)^{1/2}$, and of five nondimensional parameters, namely, the mass ratio, μ, the inertance ratio, β, the TMDI frequency ratio, ν, the TMDI damping ratio, ξ, and the primary structure inherent damping ratio ξ^*. These parameters are defined in terms of the generalized primary structure properties and the TMDI properties as

$$\mu = \frac{m_{TMDI}}{m^*},\ \beta = \frac{b}{m^*},\ \nu = \frac{\sqrt{k_{TMDI}/(m_{TMDI}+b)}}{\omega_1},\ \xi = \frac{c_{TMDI}}{2\sqrt{(m_{TMDI}+b)k_{TMDI}}},\ \text{and}\ \xi^* = \frac{c^*}{2\sqrt{m^*k^*}}. \tag{9}$$

Clearly, the equations of motion in Equation (8) define a 2-DOF dynamical model, which approximates the response of the TMDI-equipped cantilevered continuous beam of Figure 1b in terms of the free-end displacement $z(t)$ and the secondary TMDI mass displacement $y(t)$. Importantly, the properties of the herein derived 2-DOF model depend explicitly on the flexural stiffness and mass distribution of the primary cantilevered beam structure as well as on the assumed deflected shape (mode) $\psi(x)$ through the generalized SDOF properties in Equation (6). Further, the 2-DOF model accounts for the location $x = \chi$ that the inerter connects the secondary mass to the primary structure through the modal coordinate $\psi(\chi)$. In this regard, the considered 2-DOF model encompasses the special case of a TMDI with grounded inerter (i.e., the inerter connects the TMDI mass to the ground) by setting $\chi = 0$ in Equation (8) for which $\psi(0) = 0$. The latter TMDI arrangement (with grounded inerter) has been widely studied in the literature[18,24,29,41] and corresponds to a TMD with secondary mass equal to $b + m_{TMDI}$ for force-excited primary structure. To this end, it is deemed convenient to define the nondimensional inerter connectivity ratio

$$\mathrm{CR} = \frac{h-\chi}{h}, \tag{10}$$

which will be seen to be a critical parameter for TMDI motion control performance taking values between $CR = 0$ (inerter in parallel to TMDI spring and dashpot) and $CR = 1$ (grounded inerter). Further to the TMDI with grounded inerter, the 2-DOF model can also approximate the special case of a conventional TMD with secondary mass m_{TMDI} attached to the free end of the primary structure by setting $b = \beta = 0$ in Equation (8).

2.2 | Frequency response functions

To expedite numerical work in subsequent sections, a set of nondimensional FRFs corresponding to response quantities of practical interest are herein derived analytically. To this end, the equations of motion in Equation (8) are first written in the domain of circular frequency, ω, as

$$\begin{cases} \left[1-g^2\left(1+\beta\psi(\chi)^2\right)+(\nu^2+i2g\nu\xi)(\mu+\beta)+i2g\xi^*\right]Z(\omega)+\left[g^2\beta\psi(\chi)-(\nu^2+i2g\nu\xi)(\mu+\beta)\right]Y(\omega)=\dfrac{P^*(\omega)}{k^*}, \\ \left[g^2\beta\psi(\chi)-(\nu^2+i2g\nu\xi)(\mu+\beta)\right]Z(\omega)+(\nu^2-g^2+i2g\nu\xi)(\mu+\beta)Y(\omega)=0, \end{cases} \tag{11}$$

in which $i=\sqrt{-1}$, g is the normalized frequency ω/ω_1, $Z(\omega)$ and $Y(\omega)$ are the Fourier transformed displacements $z(t)$ and $y(t)$, respectively, and $P^*(\omega)$ is the Fourier transform of the generalized load $p^*(t)$ in Equation (6). Then, by eliminating $Y(\omega)$ from Equation (11), one obtains the nondimensional FRF relating the primary structure free-end displacement to the static free-end displacement $P^*(\omega)/k^*$ given as

$$H(\omega) = \frac{Z(\omega)}{P^*(\omega)/k^*} = \frac{(\nu^2-g^2+i2g\nu\xi)(\mu+\beta)}{\left\{1-g^2\left[1+\beta\psi(\chi)^2\right]+(\nu^2+i2g\nu\xi)(\mu+\beta)+i2g\xi^*\right\}(\nu^2-g^2+i2g\nu\xi)(\mu+\beta)-\left[(\nu^2+i2g\nu\xi)(\mu+\beta)-g^2\beta\psi(\chi)\right]^2}. \tag{12}$$

In subsequent sections, the above analytical FRF is used to facilitate optimal TMDI design (tuning). Further, the nondimensional FRF of the relative displacement of the TMDI secondary mass with respect to the primary structure free-end displacement, commonly termed as TMDI stroke, is given as

$$G(\omega)=\frac{Z(\omega)-Y(\omega)}{P^*(\omega)/k^*}= \frac{g^2[\beta\psi(\chi)-(\mu+\beta)]}{\left\{1-g^2\left[1+\beta\psi(\chi)^2\right]+(\nu^2+i2g\nu\xi)(\mu+\beta)+i2g\xi^*\right\}(\nu^2-g^2+i2g\nu\xi)(\mu+\beta)-\left[(\nu^2+i2g\nu\xi)(\mu+\beta)-g^2\beta\psi(\chi)\right]^2}, \tag{13}$$

while the nondimensional FRF of the relative acceleration between the secondary mass and the primary structure at height $x=\chi$, that is, $\psi(\chi)\ddot{z}(t)-\ddot{y}(t)$, is given as

$$B(\omega)=\frac{[Z(\omega)\psi(\chi)-Y(\omega)]\omega^2}{P^*(\omega)/m^*}= \frac{\{\psi(\chi)[(\nu^2-g^2+i2g\nu\xi)(\mu+\beta)]-[(\nu^2+i2g\nu\xi)(\mu+\beta)-g^2\beta\psi(\chi)]\}g^2}{\left\{1-g^2\left[1+\beta\psi(\chi)^2\right]+(\nu^2+i2g\nu\xi)(\mu+\beta)+i2g\xi^*\right\}(\nu^2-g^2+i2g\nu\xi)(\mu+\beta)-\left[(\nu^2+i2g\nu\xi)(\mu+\beta)-g^2\beta\psi(\chi)\right]^2}. \tag{14}$$

The analytical FRFs in Equations (13) and (14) are used in the numerical part of this work for efficient calculation of the TMDI stroke, damping force, and inerter force under random excitation. This is achieved through frequency domain random vibration analysis as detailed in the next subsection.

2.3 | Random vibration analysis for white noise excitation

For the case of stochastically excited primary structure, the previous analytically derived FRFs can be readily used to calculate RMS response statistics through standard random vibration analysis in frequency domain. Specifically, consider the case of zero-mean uniformly distributed in space white noise excitation. For this excitation, response power spectral density (PSD) functions of practical interest are computed with the aid of the FRFs in Equations (12)–(14) as

$$S_z(\omega)=\frac{|H(\omega)|^2S_p(\omega)}{(k^*)^2}, S_{stroke}(\omega)=\frac{|G(\omega)|^2S_p(\omega)}{(k^*)^2}, S_v(\omega)=\frac{|\omega G(\omega)|^2S_p(\omega)}{(k^*)^2}, \text{and } S_a(\omega)=\frac{|B(\omega)|^2S_p(\omega)}{(m^*)^2}, \tag{15}$$

where $S_z(\omega)$ is the PSD of the free-end displacement of the primary structure, $S_{stroke}(\omega)$ is the PSD of the TMDI stroke, $S_v(\omega)$ is the PSD of the relative velocity between the attached mass and the cantilever free end, and $S_a(\omega)$ is the PSD of the relative acceleration between the attached mass and cantilever structure at height χ. In the above expressions, $S_p(\omega)$ is the excitation PSD given as

$$S_p(\omega)=\left(\int_0^h\psi(x)dx\right)^2W_0, \tag{16}$$

where W_0 is the constant PSD amplitude of the white noise excitation. Then, the RMS values of the free-end displacement of the primary structure, $z(t)$, attached mass stroke, $z(t)$–$y(t)$, damping force, $f_c(t)$, and inerter force, $f_b(t)$, are obtained using the expressions

$$\sigma_z=\sqrt{\int_0^{\omega_{\max}}S_z(\omega)d\omega}, \sigma_{stroke}=\sqrt{\int_0^{\omega_{\max}}S_{stroke}(\omega)d\omega}, \sigma_{fc}=c_{TMDI}\sqrt{\int_0^{\omega_{\max}}S_v(\omega)d\omega}, \text{and } \sigma_{fb}=b\sqrt{\int_0^{\omega_{\max}}S_a(\omega)d\omega}, \tag{17}$$

respectively, where $\omega_{\max}$ is a cutoff frequency above, which the PSDs in Equation (15) attain negligible values.

3 | OPTIMAL TMDI DESIGN USING THE 2-DOF SIMPLIFIED MODEL

3.1 | Optimal design for resonant harmonic loading

Consider the case of a harmonic generalized load applied to the 2-DOF model defined in the previous section with frequency equal to ω_1, that is, the natural frequency of the generalized SDOF system representing the primary structure. Arguably, this is a worse-case scenario excitation based on resonance considerations.[42] In this respect, it is deemed useful to examine the effectiveness of the TMDI to mitigate the free-end displacement $z(t)$ under resonant harmonic loading. To this aim, the magnitude of the FRF in Equation (12) at $\omega = \omega_1$ (i.e., $g = 1$) given as

$$H(\omega_1) = \frac{(\nu^2 - 1 + i2\nu\xi)(\mu+\beta)}{\left[(\nu^2 + i2\nu\xi)(\mu+\beta) - \beta\psi(\chi)^2 + i2\xi^*\right](\nu^2 - 1 + i2\nu\xi)(\mu+\beta) - \left[\beta\psi(\chi) - (\nu^2 + i2\nu\xi)(\mu+\beta)\right]^2} \tag{18}$$

is adopted to gauge TMDI motion control effectiveness. This is because $|H(\omega_1)|$ provides the ratio of the peak steady-state free-end displacement over the static displacement for resonant harmonic excitation. To ensure meaningful performance comparison for different TMDI properties, an optimal TMDI tuning problem is formulated to determine TMDI frequency, ν, and damping, ξ, properties, which minimize $|H(\omega_1)|$ given mass ratio, μ, inertance ratio, β, and inerter connectivity ratio, CR, for a primary structure with assumed deflected shape ψ and damping ratio ξ^*. In this setting, the primary TMDI design variables (DVs) can be collected in the vector $\mathbf{x}_1 = [\nu,\ \xi]^{\mathrm{T}}$ and the secondary TMDI DVs in the vector $\mathbf{x}_2 = [\beta,\mu,CR]^{\mathrm{T}}$ so that the optimal TMDI tuning problem is mathematically written as

$$\min_{\mathbf{x}_1}\{|H(\omega_1)|\}, \text{given } \mathbf{x}_2 \text{ and subjected to } \mathbf{x}_1^{\min} \le \mathbf{x}_1 \le \mathbf{x}_1^{\max}, \tag{19}$$

where the vectors $\mathbf{x}_1{}^{\min}$ and $\mathbf{x}_1{}^{\max}$ specify the lower and the upper bounds, respectively, of the search range of the two primary DVs. Note that the TMDI tuning problem in Equation (19) allows for explicit treatment of the TMD and of the TMDI with grounded inerter as special cases by taking $\beta = 0$ and $CR = 0$, respectively.

The solution of the optimization problem in Equation (19) is straightforward as the numerator of the FRF in Equation (18) becomes zero for $\nu = 1$ and $\xi = 0$, for every $\mathbf{x}_2$, ψ, and ξ^*. Still, given that in practical applications some TMDI damping will always be present in anticipation of wide-band excitations (see also next subsection), it is instructive to study the behavior of $|H(\omega_1)|$ as function of the primary DVs for different TMDI inertial and connectivity properties. To this end, Figure 2 plots $|H(\omega_1)|$ on the ν–ξ plane for TMD ($\beta = 0$) and for TMDI with $\beta = 40\%$ and different CR values. In all cases, the mass ratio is taken as $\mu = 0.1\%$, the inherent damping ratio is taken as $\xi^* = 2\%$, and the deflected shape of the primary structure is assumed to be

$$\psi(x) = 1 - \cos\left(\frac{\pi x}{2h}\right), \tag{20}$$

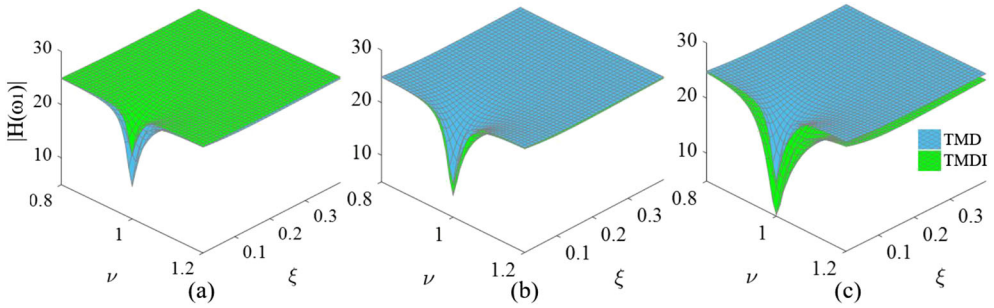

FIGURE 2 Magnitude of the nondimensional FRF, $H(\omega_1)$, in Equation (18) versus TMDI frequency ratio, ν, and damping ratio, ξ, for attached mass ratio $\mu = 0.1\%$, inertance ratios, $\beta = 0$ (TMD) and $\beta = 40\%$, and connectivity ratios, (a) 2.5%, (b) 5.0%, and (c) 7.5%

which is commonly adopted to approximate single-mode dynamic behavior of cantilevered structures whose response is dominated by their first-mode shape.[43] It is seen that the global $|H(\omega_1)|$ minimum is reached at $\nu = 1$ as $\xi \to 0$ and that the TMDI becomes more effective than TMD throughout the primary variables design plane as CR increases. The latter observation is practically important as it suggests that connecting the inerter further away from the free end of the primary structure enhances TMDI motion control for resonant harmonic loading even for nonoptimal (i.e., $\xi > 0$) TMDI damping ratios.

Further light on the optimal TMDI design for resonant harmonic loading is shed by examining numerical data in Figure 3 where $|H(\omega_1)|$ is plotted against TMDI frequency ν for three different secondary mass ratios $\mu = [0.1\%, 0.2\%, 0.3\%]$, inertance ratios $\beta = [0, 20\%, 40\%]$, and connectivity ratios $CR = [2.5\%, 5.0\%, 7.5\%]$. A fixed arbitrarily taken value of TMDI damping ratio $\xi = 5\%$ is taken, while $\xi^* = 2\%$ and the deflected shape of Equation (20) is assumed. It is seen that improved free-end displacement reduction at a wider band of frequencies around the optimal value $\nu = 1$ is achieved as the inertance ratio β and/or the connectivity ratio CR increase. On the antipode, the increase of the secondary mass has negligible effect to the motion control performance of the TMDI, though it is significant (beneficial) for the TMD. Notably, similar trends on motion control performance of optimally designed TMDI have been reported in previous works, which considered lumped-mass primary structures under earthquake and wind excitations.[25,33] These similarities indicate the capability of the simplified 2-DOF model of Section 2.1, derived from a primary structure with continuously distributed mass and stiffness properties, to capture the salient dynamics of TMDI-equipped cantilevered structures as well as to facilitate optimal TMDI tuning.

3.2 | Optimal design for white noise excitation

Turning the attention to mitigating primary structure motion to white noise excitation, TMDI optimal tuning is sought in the second norm, H_2, sense. Specifically, the primary DVs in vector $\mathbf{x}_1$ are determined to minimize the area under

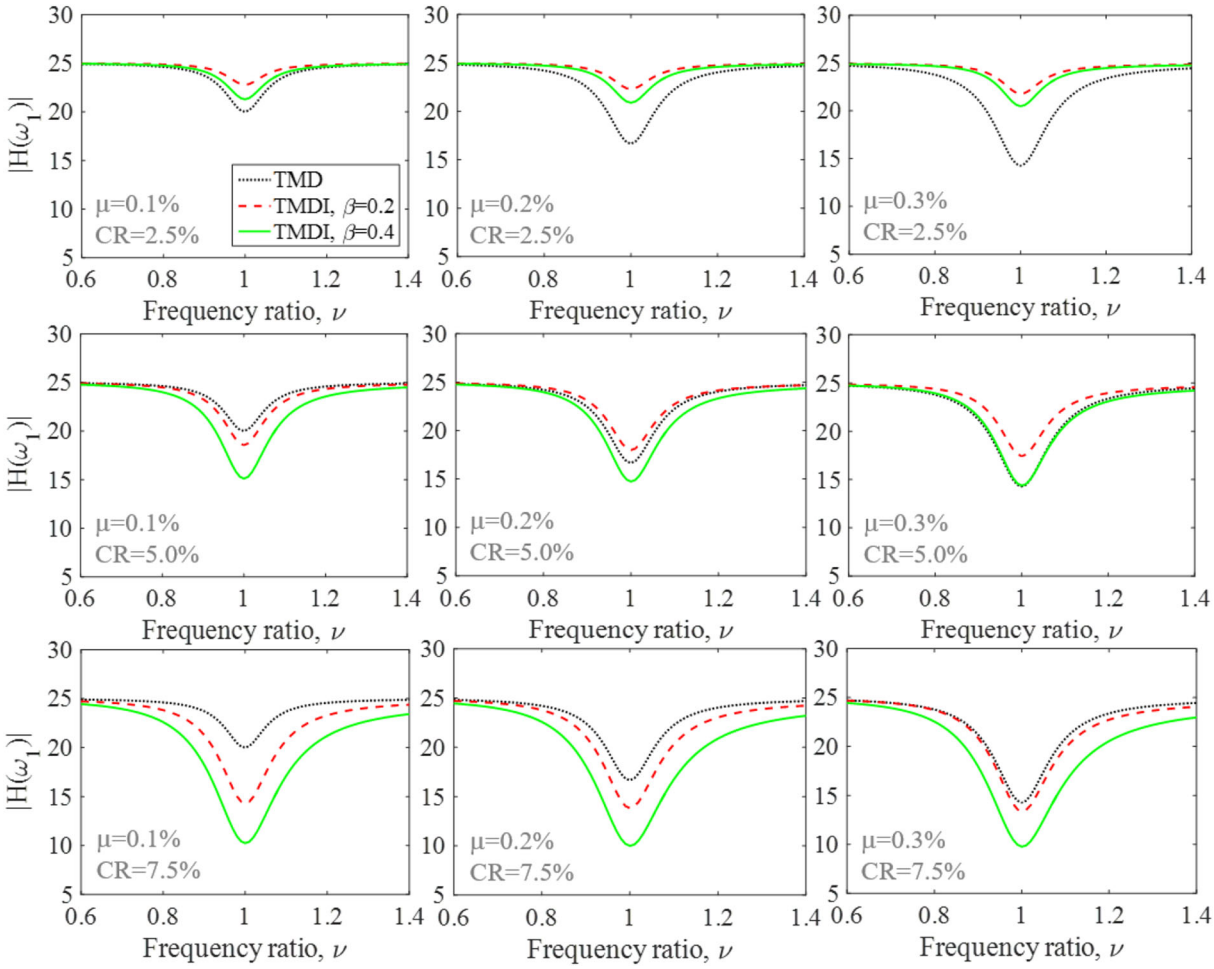

FIGURE 3 Magnitude of the nondimensional FRF, $H(\omega_1)$, in Equation (18) versus TMDI frequency ratio for various secondary mass ratios, μ, inertance ratios, β, and connectivity ratios, CR

the square magnitude of the nondimensional FRF in Equation (12) (objective function [OF]) for given secondary DVs in vector $\mathbf{x}_2$ and for assumed primary structure deflected shape ψ and damping ratio ξ^*. The underlying optimization problem is mathematically written as

$$A_{\min} = \min_{\mathbf{x_1}} \left\{ \underbrace{\int_0^{\omega_{\max}} |H(\omega)|^2 d\omega}_{\text{objective function (OF)}} \right\} \text{given } \mathbf{x}_2 \text{ and subjected to } \mathbf{x}_1^{\min} \le \mathbf{x}_1 \le \mathbf{x}_1^{\max}. \tag{21}$$

The solution to the above problem is nontrivial, and herein, pattern search[44] is employed to find numerically $\mathbf{x}_1$ that yields the minimum, $A_{\min}$, value of the OF. For computational efficiency, a custom-made pattern search algorithm with iteratively narrowing search range in a stepwise manner is hard coded in MATLAB®. In all the ensuing numerical work, the initial search range in solving the optimization problem in Equation (21) is taken as $\mathbf{x_1}^{\min} = [0.0, 0.0]^{\mathrm{T}}$ and $\mathbf{x_1}^{\max} = [2.0, 2.0]^{\mathrm{T}}$. This initial search range is iteratively narrowed around the ν and ξ values, which minimize the OF in the previous step, until the difference of $A_{\min}$ between two successive steps becomes smaller than a prespecified tolerance set equal to 10^{-2}.

For numerical illustration, Figure 4 plots the OF in Equation (21) on the primary DV plane computed in three different successive steps/iterations of the pattern search algorithm for $\mathbf{x}_2 = [40\%, 0.1\%, 7.5\%]^{\mathrm{T}}$, $\xi_1 = 2\%$, and primary structure deflected shape in Equation (20). Optimal values $\nu(j)$, $\xi(j)$, and $A_{\min}(j)$ for $j = 1,2,3$ iterations are indicated in the plots. It is seen that the algorithm converges fast and that the OF is convex near the optimum, exhibiting a single (global) minimum. The same behavior is noted in all cases examined later in this work. Moreover, in the inlet of Figure 4c, the magnitude of the normalized FRF in Equation (12) for the optimally designed TMDI is plotted to demonstrate the nature of the achieved optimality. It is seen that the free-end displacement FRF exhibits two distinct peaks of almost equal height with a local minimum (valley) attained roughly at the uncontrolled fundamental frequency. These two peaks correspond to the shifted vibration mode of the primary structure and the TMDI mode.

Further to Figure 4c, Figure 5 plots the magnitude of the FRF in Equation (12), $|H(\omega)|$, for optimally designed TMDIs to white noise excitation for the same $\mathbf{x}_2$ properties and primary structure considered in Figure 3. Evidently, increased inerter and connectivity ratios are beneficial to the TMDI capability to mitigate primary structure motion for white noise excitation just as for resonant harmonic excitation, while the mass ratio has negligible effect.

4 | GEOMETRIC SHAPE VARIATION OF PRIMARY STRUCTURE

4.1 | Geometric shape definition and derivation of fundamental mode shapes

Having established the applicability and usefulness of the simplified 2-DOF model presented in Section 2 to support optimal TMDI tuning for motion control of cantilevered primary structures, the attention is turned to leveraging this

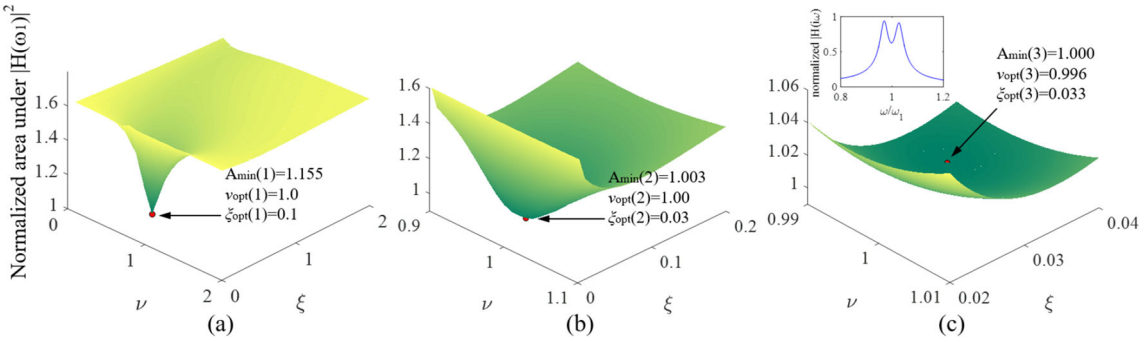

FIGURE 4 Iterative pattern search algorithm illustration for solving the optimization problem in Equation (21) for TMDI with mass ratio $\mu = 0.1\%$, inertance ratio $\beta = 40\%$, and connectivity ratio $CR = 7.5\%$, and primary structure with $\xi^* = 2\%$ and deflected shape in Equation (20): (a) first iteration, (b) second iteration, and (c) third iteration

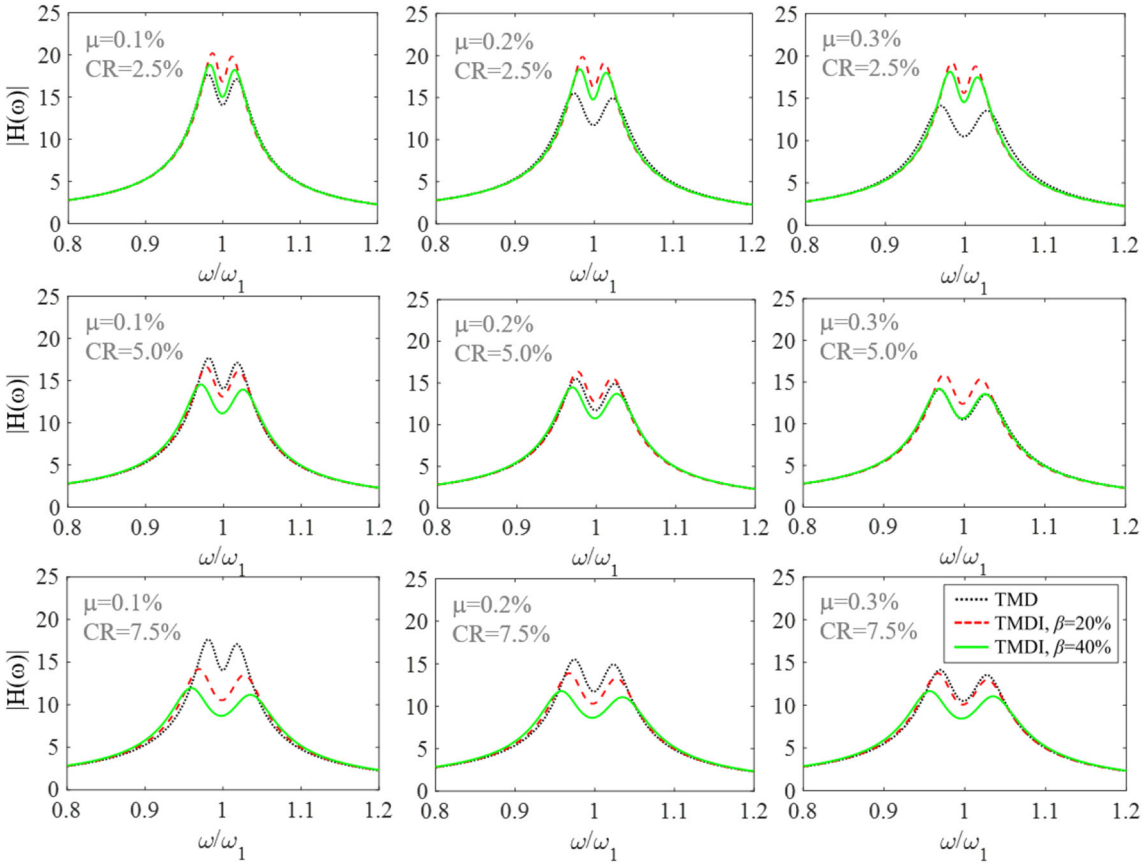

FIGURE 5 Magnitude of the nondimensional FRF, $H(\omega)$, in Equation (12) for optimally designed TMDIs to white noise excitation for various secondary mass ratios, μ, inertance ratios, β, and connectivity ratios, CR

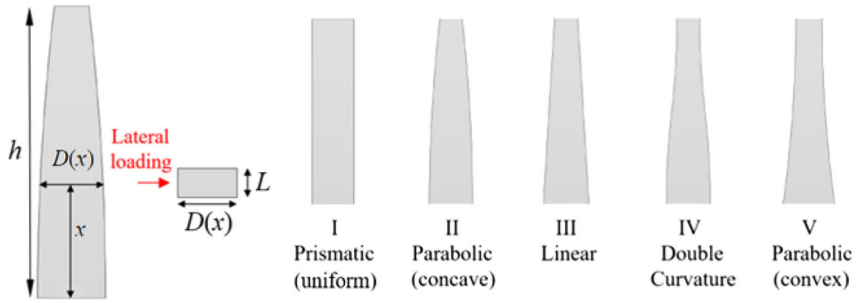

FIGURE 6 Considered geometric shapes of cantilevered beam-like primary structures

model for investigating the influence of the primary structure geometry to the TMDI vibration suppression effectiveness. To this aim, cantilevered beams with solid rectangular cross section, height h, constant width L, and varying depth $D(x)$ with height are considered as shown in Figure 6. The continuously varying depth allows to define beams with different smoothly tapered shapes inspired by real-life structures such as industrial chimneys,[6] slender towers supporting renewable energy generation,[8,45] and tall buildings.[4,5] Specifically, beams with five different geometric shapes shown in Figure 6 are defined through the analytical expressions of the depth profiles, $D(x)$, reported in Table 1. The uniform shape "I" has constant depth profile assuming a square cross section. The nonconstant depth profiles of the other four geometric shapes are specified with the aid of the depth ratio $R = D(0)/D(h)$ (i.e., base depth over free-end depth). Purposely, the base depth, $D(0)$, is defined as a function of R (see Table 1) such that all shapes have the same total volume

TABLE 1 Analytical definition of primary structure geometric shapes in Figure 6 through the depth $D(x)$ and the depth ratio $R = D(0)/D(h)$

Shape	Description	Depth at the base $D(0) = D_0$	Depth at height x $D(x)$	Depth at the tip $D(h)$
I	Uniform	L	L	L
II	Parabolic (concave)	$3L/(2 + 1/R)$	$D_0 + D_0(1/R - 1)(x/h)^2$	D_0/R
III	Linear	$2L/(1 + 1/R)$	$D_0 + D_0(1/R - 1)x/h$	
IV	Double curvature	$2L/(1 + 1/R)$	$D_0 + 1/2D_0(1/R - 1)[1 - \cos(\pi x/h)]$	
V	Parabolic (convex)	$3L/(1 + 2/R)$	$D_0 + D_0(1 - 1/R)[(x/h)^2 - 2(x/h)]$	

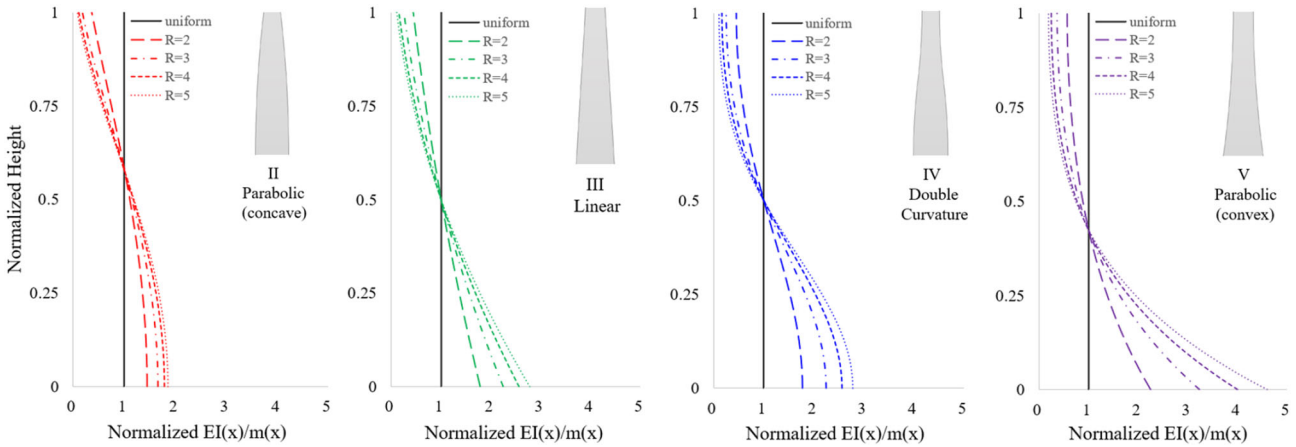

FIGURE 7 Rigidity over mass distribution plots for all considered geometric shapes (depth profiles in Table 1) and for various depth ratios R of cantilevered beam-like primary structures

for any value of R. This consideration allows for establishing beams with different height-wise mass and flexural rigidity distributions expressed as

$$m(x) = \rho L D(x) \quad \text{and} \quad EI(x) = \frac{ELD^3(x)}{12}, \tag{22}$$

respectively, but with the same total mass equal to $\rho h L^2$, where ρ is the mass density. In this regard, these beams constitute a practically meaningful set of parametrically defined primary structures for the purpose of assessing comparatively the TMDI motion control effectiveness. This is because they attain different dynamic/modal properties, which do influence TMDI efficacy, but have equal total weight and material usage, which are directly linked to sustainability considerations in construction.[1]

To provide an insight into the relative variation of mass and flexural rigidity distributions of the primary structures in Figure 6, Figure 7 plots the ratio $EI(x)/m(x)$ (i.e., flexural rigidity over mass) for different values of the depth ratio R and for all four nonuniform geometric shapes. These plots are normalized by the constant ratio $EI/m = EL^2/12\rho$ of the uniform shape. In all the panels of Figure 7, the same reference continuous curve corresponding to the uniform shape ($R = 1$) is included to facilitate comparisons. It is seen that for all shapes (depth profiles $D(x)$), an increase in the depth ratio R results in higher values of $EI(x)/m(x)$ towards the base of the structure and lower values towards the free end of the structure. Therefore, an increase of R defines primary structures that become increasingly more flexible with height. Further, as shapes evolve from "II" to "V," the rate of change of $EI(x)/m(x)$ with height reduces faster; that is, the primary structure becomes more flexible with height at a faster rate while the value $[EI(h)/m(h)]/[EI(0)/m(0)]$ reduces. In fact, for shapes "IV" and "V," the ratio $EI(x)/m(x)$ becomes practically constant $x/h > 0.80$ and $x/h > 0.75$,

respectively. Notably, these differences in the distribution of $EI(x)/m(x)$ with height affect the properties of the primary structure mode shapes as discussed later in this section.

Regardless of their geometric shape, the assumption that the dynamic response of the primary structure is dominated by the first/fundamental mode shape, $\varphi_1(x)$, is made, which is reasonable for slender structures. In this respect, the simplified 2-DOF model of Section 2 can be used in conjunction with the primary structures in Figure 6 by using the mass and flexural rigidity distributions of Equation (22) in Equation (6) and by setting $\psi(x) = \varphi_1(x)$. For the purposes of this work, the fundamental mode shape $\varphi_1(x)$ of the uncontrolled primary structures is numerically approximated using a FE approach. This is achieved by discretizing the primary structure using 40 tapered equal-length linear Euler–Bernoulli beam elements. Then, a 41-DOF planar dynamic model is derived involving only one lateral translational DOF per FE node grid along the horizontal load direction in terms of a diagonal mass matrix and a full stiffness matrix. The mass matrix is formed by lumping the own mass of the elements at the nodes, while the stiffness matrix is constructed using standard static condensation to eliminate vertical and rotational DOFs at each FE node. Next, standard modal analysis is conducted to obtain the fundamental mode shape vector $\boldsymbol{\varphi}_1 \in \mathbb{R}^{41 \times 1}$. The central difference method is used to obtain numerically the second derivative of the mode shape vector (modal curvature), and the standard trapezoid quadrature rule is used to determine the integrals in defining the generalized primary structure properties in Equation (6).

The influence of the geometric shape of the primary structure to its fundamental mode is qualitatively seen in Figure 8a,b. In Figure 8a, numerically derived fundamental modes are plotted for all five geometric shapes of Figure 6 and for the same ratio $R = 3$ (except for the uniform-shaped structure, which can only attain $R = 1$), while in Figure 8b, fundamental modes for shapes "I" and "V" with different depth ratios $R = 2$, 3, 4, and 5 are plotted. It is observed that as geometric shapes vary from "II" towards "V" for fixed R and as the ratio R increases for fixed shape, the convexity of the modes increases. This is readily justified by the fact that the ratio $EI(x)/m(x)$ takes on higher values (i.e., is always heavier distributed) towards the base of the primary structure and reduces faster with height as R increases and/or as shapes vary from "II" to "V" as previously discussed in view of Figure 7. In this work, the average modal curvature along the height of the structure is used as an intuitive scalar quantitative metric to measure the convexity of the fundamental modal shape. The variation of this novel metric for the four nonuniform primary structures and for $R = 2$, 3, 4, and 5 is reported in Figure 8c in which ordinates are normalized by the average curvature of the uniform primary structure. This is an important consideration for the purposes of this work as it will be seen, in subsequent sections, that the average modal curvature of the primary structure correlates well with the TMDI motion control potential.

4.2 | Verification of the simplified 2-DOF model for optimal TMDI design and performance assessment

Besides approximating the dynamic response of the primary structure via a single-mode shape, a major simplifying assumption made in the 2-DOF model defined in Section 2 is that it does not account for the structure–TMDI

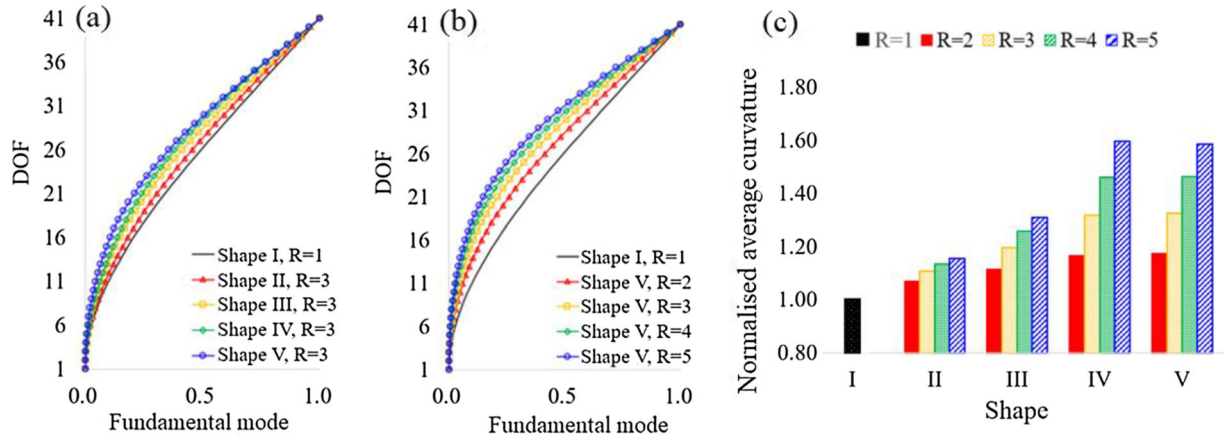

FIGURE 8 Numerically derived fundamental mode shapes and average modal curvature for primary structures with different depth profiles (shapes) and depth ratios R

interaction effect to this mode shape. Indeed, the inclusion of the TMDI alters locally the fundamental mode shape of the primary structure, which, in turn, may affect the effectiveness of the optimal TMDI tuning if using the simplified 2-DOF model for the task. Thus, it is herein deemed important to verify the accuracy of the 2-DOF model for optimal TMDI tuning vis-à-vis a more detailed model that can capture the structure–TMDI coupling as well as the effects of higher modes. For the same reason, it is also deemed essential to verify the accuracy of the 2-DOF model for structural performance assessment.

At this juncture, note that the combination of large R, β, and CR values leads to higher influence of the TMDI to mode shapes since a large R specifies primary structures with a more flexible upper part while large β and CR result in higher magnitude dashpot and inerter forces exerted to the primary structure (see Figure 13 later in the paper). Therefore, structures with high ratio $R = 5$ for shapes II–V and large TMDI inertance, $\beta = 40\%$, and $CR = 7.5\%$ are used for the verification of the 2-DOF accuracy. For each structure, two different dynamic systems are considered to determine the FRF $H(\omega)$ used in the OF for optimal tuning. The first system is the 2-DOF model in Section 2 in which $\psi(x)$ is set equal to the fundamental mode shape of the uncontrolled primary structure. This mode shape is estimated through modal analysis using the 41-DOF FE model as detailed in Section 4.1. For this system, the $H(\omega)$ is determined using Equation (12). The second system uses directly the 41-DOF FE modeling of the primary structure, which is augmented by an additional DOF for the TMDI following the formulation of Giaralis and Petrini.[31] The resulting 42-DOF model accounts for primary structure–TMDI interaction explicitly, while $H(\omega)$ is determined using the frequency domain approach in Giaralis and Petrini.[31] Next, two different sets of optimal TMDI primary DV values, ν_{opt} and ξ_{opt}, are computed by solving the optimization problem in Equation (21) using the $H(\omega)$ from the two different systems (the 2-DOF and the 42-DOF).

Table 2 reports the percentage difference of the two sets of optimal TMDI tuning parameters for all structures considered. In the same table, the deviation to the structural performance due to adopting different sets of TMDI tuning parameters for each structure is also reported, measured in terms of RMS free-end displacement percentage difference obtained from 42-DOF detailed models under white noise excitation. It is evidenced that the simplified 2-DOF model is sufficiently accurate to be used for TMDI optimal tuning since errors to the tuning parameters are less than 0.2% for all considered structures causing deviations to structural performance of 1% or less. Moreover, Table 2 furnishes differences to structural performance obtained by using the simplified and the detailed models and adopting the corresponding sets of TMDI tuning parameters. It is seen that percentage differences are less than 2% across the board. In view of these small differences, the 2-DOF model is used for optimal TMDI tuning and comparative performance assessment of TMDI-equipped primary structures in all the ensuing numerical work. Note that this consideration expedites significantly the computational work given that the evaluation of $H(\omega)$ for the 42-DOF model involves multiplications and inversion of 42-by-42 full matrices, which are computationally much more demanding than the evaluation of $H(\omega)$ through Equation (12). Hence, the practical merit of the model in Section 2 is established for optimal TMDI tuning of generic cantilevered structures with dominant fundamental mode.

5 | PERFORMANCE ASSESSMENT OF TMDI-EQUIPPED STRUCTURES WITH DIFFERENT GEOMETRIC SHAPES

In this section, the influence of primary structure geometric shape to the motion control effectiveness of TMDI is assessed through a parametric numerical investigation, involving primary structures of different geometric shapes

TABLE 2 Absolute percentage differences of optimal TMDI tuning parameters and of RMS free-end displacements using 42-DOF detailed FE models and 2-DOF simplified models of TMDI-equipped primary structures with $\mu = 0.3\%$, $\beta = 40\%$ and $CR = 7.5\%$

	Primary structure				
	I ($R = 1$)	**II ($R = 5$)**	**III ($R = 5$)**	**IV ($R = 5$)**	**V ($R = 5$)**
ν_{opt}	0.00%	0.05%	0.13%	0.09%	0.16%
ξ_{opt}	0.00%	0.00%	0.00%	0.00%	0.00%
RMS free-end displacement deviation	0.01%	0.49%	0.61%	0.30%	1.05%
RMS free-end displacement performance	1.88%	1.15%	1.22%	1.42%	1.69%

Note: Optimal tuning for white noise excitation is considered.

characterized by the depth ratio $R = D(0)/D(h)$ and the depth profile $D(x)$ in Table 1 and Figure 6. To this aim, TMDIs with various μ, β, and CR properties are optimally tuned for resonant harmonic excitation or for white noise excitation (as indicated in the text and figure captions) by solving the optimization problem in Equation (19) or (21), respectively. In all structures investigated, $\xi^* = 2\%$ inherent structural damping is assumed. To expedite computations, the 2-DOF model of Section 2 with deflected shape $\psi(x)$ equal to the fundamental mode shape of the primary structure is used for TMD(I) tuning and for obtaining response quantities of interest throughout this section for the above excitations. Fundamental mode shapes are computed through modal analysis applied to FE models of the primary structures as detailed in Section 4.2.

5.1 | Influence of depth ratio R to free-end displacement

First, attention is focused on investigating the influence of the depth ratio $R = D(0)/D(h)$ of the primary structure to the TMDI motion control efficacy. This is supported by plotting in Figure 9 the RMS free-end displacement of optimal TMDI-equipped structures against CR for fixed depth ratios $R = 2$, 3, 4, and 5 and for each of the geometric shapes II–V in Figure 6, separately. The same TMDI mass and inertance are considered for all structures of each panel of Figure 9, taken as $m_{TMDI} = 0.1\% \times m^*_{Avg}$ and $b = 40\% \times m^*_{Avg}$, respectively, where m^*_{Avg} is the average generalized mass m^* in Equation (6) of all the primary structures studied in all the panels of Figure 9. These assumed inertial values are representative of low mass/weight and high inertance TMDIs, which were found to be quite effective and advantageous over TMDs in earthquake[25] and wind[31] engineering applications as they relax requirements for large secondary mass and reduce significantly the kinematics of the secondary mass. Both considerations are practically important: the former leads, ultimately, to more lightweight and, therefore, economic absorbers; the latter reduces needs for space/clearance to accommodate the absorber, as well as the cost of energy dissipation devices (dampers)

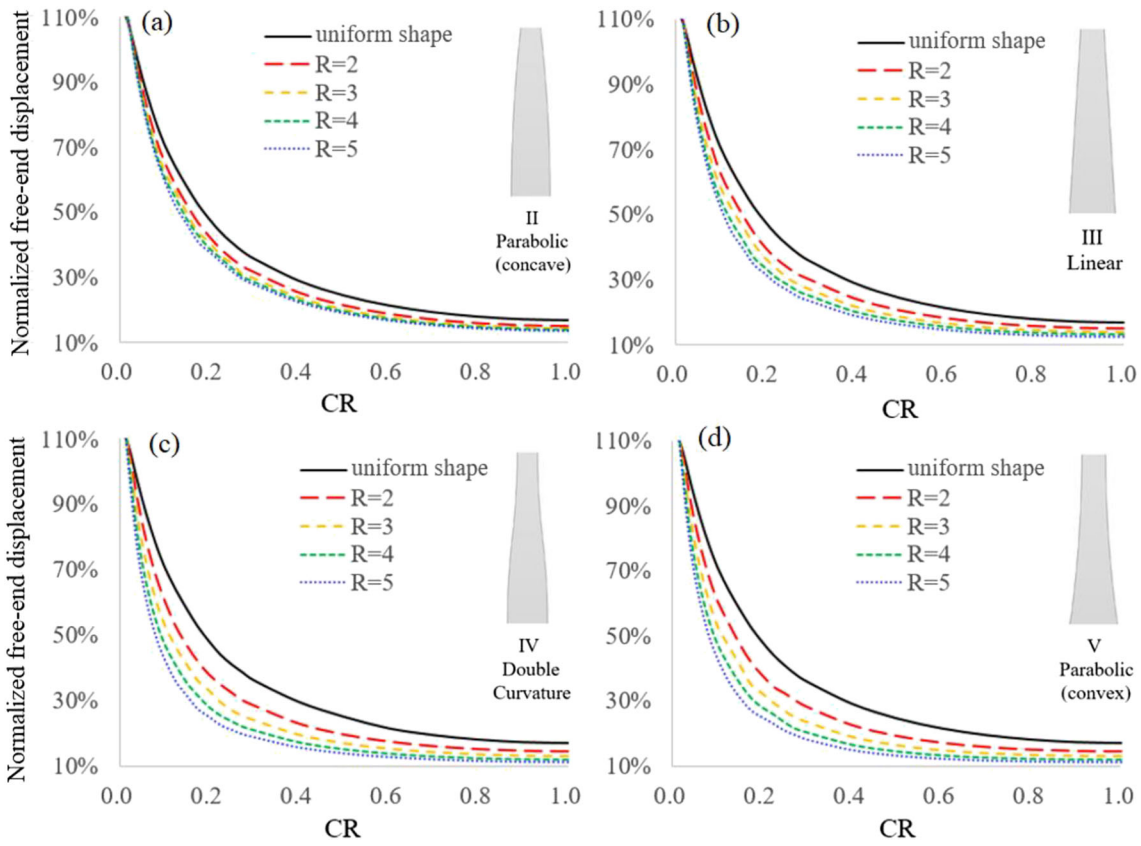

FIGURE 9 RMS free-end displacements of white noise excited TMDI-equipped structures for attached mass $m_{TMDI} = 0.1\% \times m^*_{Avg}$ and inertance $b = 0.40 \times m^*_{Avg}$ for different geometric shapes and depth ratios normalized by the corresponding displacements of optimal TMD-equipped structures and plotted against CR. Optimal tuning is for white noise excitation

whose cost increases with the stroke (relative displacement between primary structure and secondary mass). For each structure, TMDI is optimally tuned for white noise excitation using Equation (21). Further, the reported RMS free-end displacements in Figure 9 are normalized by the RMS free-end displacement of the same primary structure equipped with a same-mass TMD, which is optimally tuned by solving Equation (21) for $b = 0$. In all the panels of Figure 9, the same reference continuous curve corresponding to the uniform shape ($R = 1$) is included to facilitate comparisons.

It is seen that improved vibration suppression is achieved monotonically as *CR* increases (i.e., as the inerter links the secondary mass further away from the free end) for all geometric shapes and *R* values and, thus, for all different primary structure mode shapes. In this regard, best performance is always achieved for TMDIs with grounded inerter ($CR = 100\%$), which have been widely studied in the literature.[18,19,24,25,29,30,36] However, this performance improvement saturates with *CR* quickly for all structures such that little improvement is achieved for $CR > 30\%$. Further, for relatively small *CR* values (less than about 3%), the TMD outperforms the TMDI (normalized free-end displacement is higher than 100%). All the above observations agree with the trends reported in previous numerical studies examining various TMDI-equipped lumped-mass models of different benchmark building structures exposed to wind or earthquake excitations.[21,25,26,28,31,33] Hence, it is safe to conclude that these trends are applicable to any type of cantilevered primary structure, and it is always beneficial to connect the second terminal of the inerter as further away from the free end of the primary structure as structurally and economically feasible.

More importantly, reported data in Figure 9 evidence that optimal TMDI performance improves monotonically over a same-mass TMD as the depth ratio *R* increases for fixed *CR* value and for any geometric shape considered. This improvement is more substantial for lower *CR* values. This novel finding suggests that the TMDI becomes more effective as the upper part of cantilevered primary structures becomes more flexible (see discussion in view of Figure 7) for same total structural weight. In this regard, from the structural design viewpoint, the *CR* can be traded for tapering of the primary structure geometric shape in achieving a desired target structural performance for fixed inertial TMDI parameters (i.e., mass m_{TMD} and inertance *b*). For instance, for shape "V" in Figure 9d, the required *CR* for a TMDI with $m_{TMDI} = 0.1\% \times m^*_{Avg}$ and $b = 40\% \times m^*_{Avg}$ to achieve 50% better performance than a TMD with the same mass reduces from 18% to 11% as the depth ratio increases from $R = 2$ to $R = 4$. In the first instance, this consideration is practically useful as it leads to more lightweight vibration absorbers and, thus, more economical since the attached mass is proportional to the up-front TMD(I) cost.[26] The consideration is also beneficial in applications where connecting the inerter much below the top of the structure is practically challenging such as in the case of tall buildings discussed in Wang and Giaralis[38] and Kaveh et al.[28] In this respect, increasing the depth ratio *R* of the primary structure (or more generally designing the primary structure such that the flexural rigidity over mass ratio, $EI(x)/m(x)$, reduces faster with height) widens the applicability of the TMDI over the TMD. As an example, note that for shape "IV" in Figure 9c, the critical *CR* value beyond which the TMDI outperforms the TMD is 7.4%, 5.1%, and 2.75% for depth ratios $R = 1$ (uniform), $R = 2$, and $R = 5$, respectively.

5.2 | Influence of depth profile (primary structure shaping) to free-end displacement

In this section, the attention is turned to quantifying the influence of the depth profile, $D(x)$, of primary structures on the TMDI motion control potential. For this purpose, Figures 10 and 11 plot peak steady-state displacement under resonant harmonic excitation and RMS free-end displacement under white noise excitation of primary structures with different geometric shapes equipped with TMDIs tuned for resonant harmonic and for white noise excitations, respectively. Displacement values are normalized by the corresponding displacements of optimally tuned TMD-equipped structure. In each horizontal row of panels of these two figures, 17 different primary structures are considered with the same TMDI mass and inertance (though different horizontal rows use different μ and β ratios for comparison) equal to $m_{TMDI} = \mu \times m^*_{Avg}$ and $b = \beta \times m^*_{Avg}$, respectively, where m^*_{Avg} is the averaged generalized mass in Equation (6) across the 17 primary structures. TMDI parameters for resonant harmonic excitation are set as $\nu = 1$ and $\xi = 5\%$, while TMDI parameters for white noise excitation are determined numerically by solving Equation (21). A sample of optimal TMDI parameters, ν_{TMDI} and ξ_{TMDI}, for white noise excitation and for $\mu = 0.3\%$, $\beta = 40\%$, and three *CR* values (2.5%, 5.0%, and 7.5%) are plotted in Figure 12.

It is seen that, for sufficiently large *CR* values (5.0% and 7.5%), the TMDI motion control potential improves over the TMD as the depth profile (shape) of the primary structure changes from shape "II" towards shape "V" for any fixed *R* value and for both resonant harmonic and white noise excitations. With reference to Figure 8c, this trend suggests

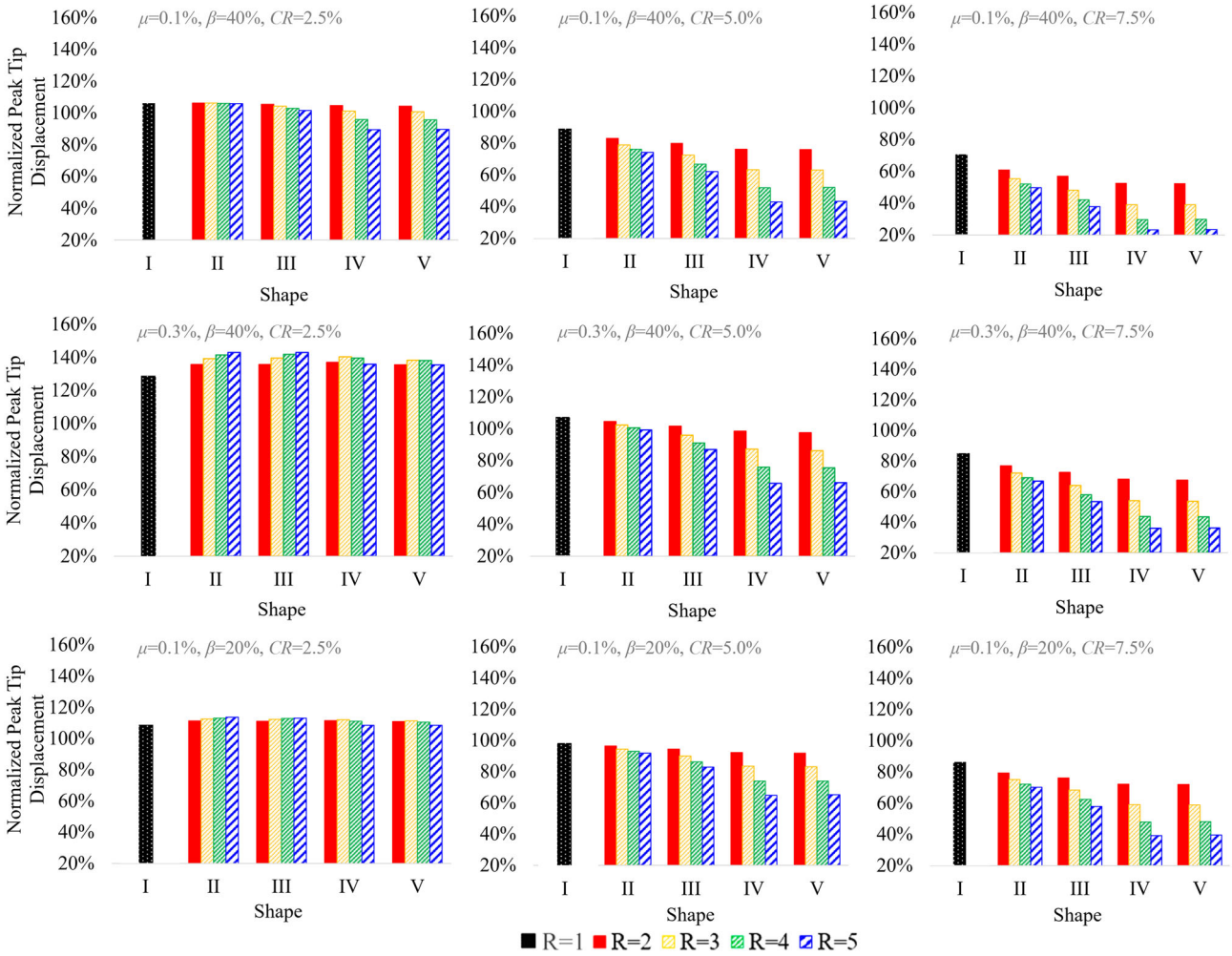

FIGURE 10 Peak free-end displacement of TMDI-equipped structures under resonant harmonic excitation for attached mass $m_{TMDI} = \mu \times m^*_{Avg}$, inertance $b = \beta \times m^*_{Avg}$, and various inerter connectivity ratios, *CR*, primary structure shapes, and depth ratios *R*. Values are normalized by the corresponding displacement of optimal TMD-equipped structures. Optimal tuning is for resonant harmonic excitation

that improved TMDI performance is achieved as the average modal curvature of the primary structure increases or, equivalently, as the fundamental mode shape of the uncontrolled structure becomes more convex (see Figure 8a,b). The latter is accomplished by shaping the structures such that the flexural rigidity over mass ratio, $EI(x)/m(x)$, reduces faster with height (see Figure 7). To elaborate on this point, Figure 13 plots the peak and RMS free-end displacements for resonant harmonic and white noise excited structures versus the average modal curvature of Figure 8c in the upper and lower rows of panels, respectively, corresponding to the middle row of panels of Figures 10 and 11, separately. It is seen that, for $CR \geq 5.0$, the TMDI performance improves linearly with the average modal curvature at a similar rate (slope) for all considered shapes and as *R* values increase, which establishes the beneficial effect of the average modal curvature in TMDI-equipped cantilevered structures.

At the same time, it is also evidenced in Figure 10 that the improvement of the TMDI motion control effectiveness over the TMD due to a change to the depth profile becomes more substantial for larger depth ratios. This is readily attributed to the fact that *R* influences the value of $[EI(h)/m(h)]/[EI(0)/m(0)]$ in a direct manner. For example, the improvement of TMDI performance over TMD for harmonic excitation between primary structure shapes "II" and "V" for the case of $\mu = 0.1\%$, $\beta = 40\%$, and $CR = 5.0\%$ (Figure 10) is only 7.0% (from 17.2% to 24.2%) for $R = 2$ compared to a much higher 24.0% (from 23.8% to 47.8%) for $R = 4$. Moreover, TMDI performance benefits more significantly by an increase to *R* for depth profiles exhibiting faster reduction of the $EI(x)/m(x)$ ratio with height (i.e., shapes "IV" and

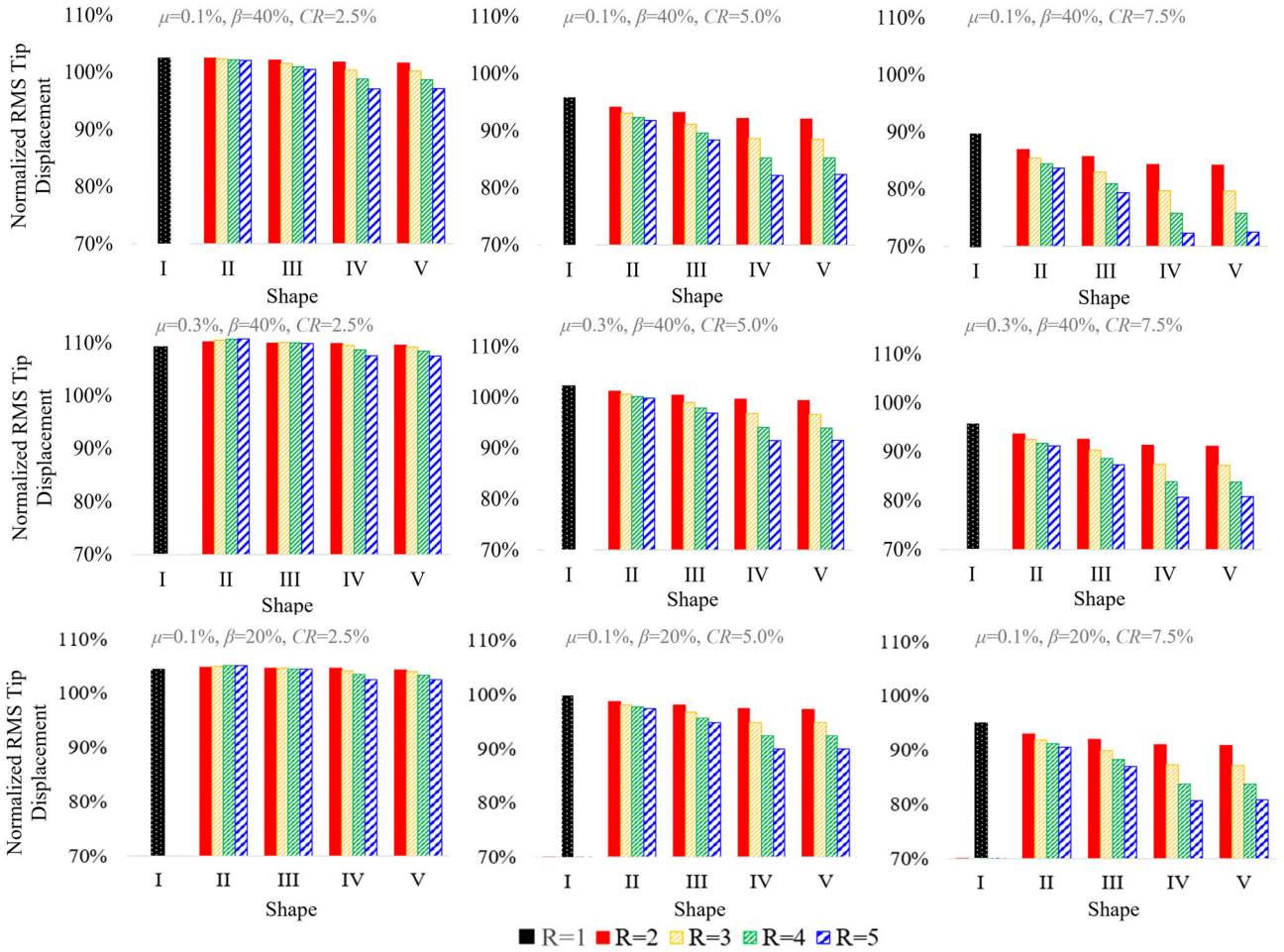

FIGURE 11 RMS free-end displacement of TMDI-equipped structures under white noise excitation for attached mass $m_{TMDI} = \mu \times m^*_{Avg}$, inertance $b = \beta \times m^*_{Avg}$, and various inerter connectivity ratios, *CR*, primary structure shapes, and depth ratios *R*. Values are normalized by the corresponding displacement of optimal TMD-equipped structures. Optimal tuning is for white noise excitation

"V"). For instance, as R increases from 2 to 4, the TMDI relative performance to TMD improves by only 6.6% (from 17.2% to 23.8%) for shape "II" as opposed to 23.6% (from 24.2% to 47.8%) for shape "V" for the previous TMDI case and harmonic resonant excitation.

Still, for the relatively low $CR = 2.5\%$ value (first column of panels in Figures 10 and 11), the TMD outperforms the TMDI except for shapes IV and V with $R = 4$ and 5 and for the combination of large inertance $\beta = 40\%$ and small secondary mass $\mu = 0.1\%$. With regard to the spectral content of the excitation, a comparison between Figures 10 and 11 shows that optimal TMDIs are more effective in suppressing structural displacement response due to harmonic excitation than white noise excitation than same-mass TMDs. For example, the TMDI with $\mu = 0.1\%$, $\beta = 40\%$, and $CR = 5.0\%$ achieves a 36.9% improvement in reducing the peak free-end displacement under harmonic excitation (Figure 10) as opposed to a mere 11.5% improvement in reducing the RMS free-end displacement under white noise excitation (Figure 11) for the primary structure shape "V" with $R = 3$. As a final remark, it is noted that for all shapes and depth ratios, the relative motion control effectiveness of TMDI over TMD improves significantly by increasing the inertance for both excitations, which can be seen by comparing the upper vis-à-vis the bottom rows of panels in Figures 10 and 11. On the other hand, this improvement reduces with the attached mass increasing, as seen by comparing the upper vis-à-vis the middle rows of panels in Figures 10 and 11. These trends confirm that, irrespective of the primary structure shape, the TMDI attached mass can be traded off to inertance in order to achieve some target structural performance as has been exhaustively demonstrated and discussed in the literature.[23,33]

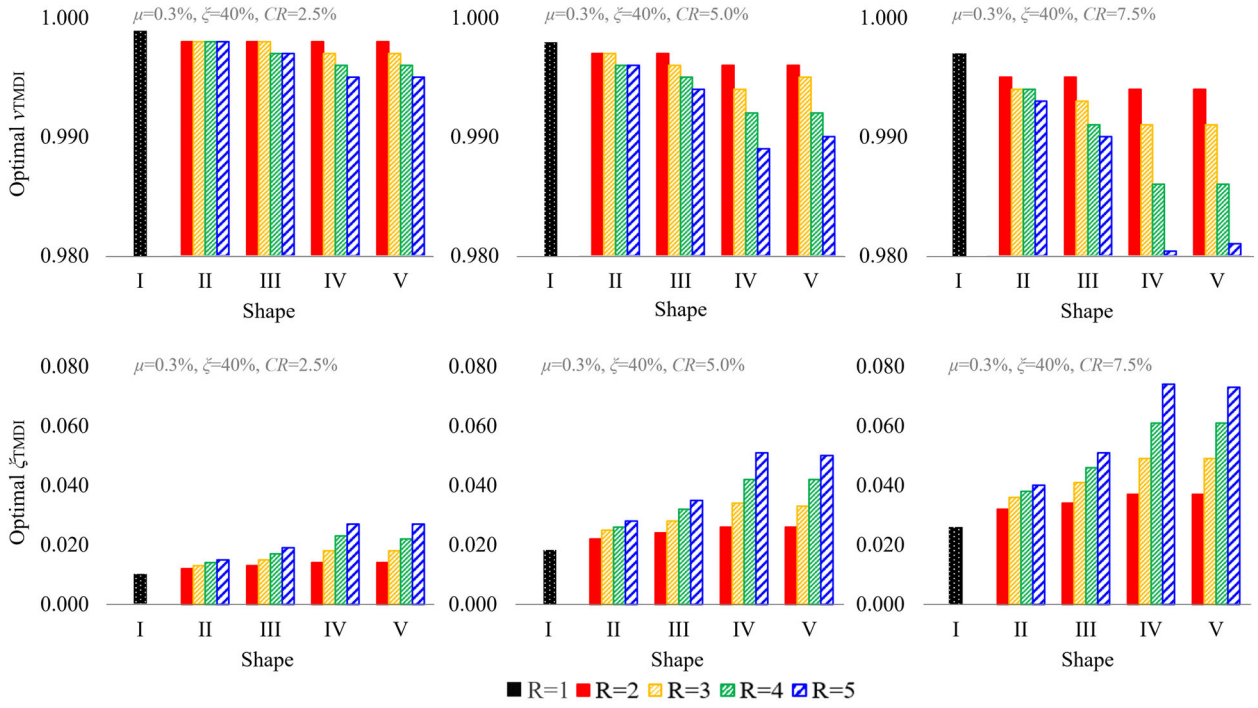

FIGURE 12 Optimal TMDI tuning parameters for white noise excitation, attached mass $m_{TMDI} = 0.3\% \times m^*_{Avg}$, inertance $b = 0.4 \times m^*_{Avg}$, various inerter connectivity ratios, *CR*, primary structure shapes, and depth ratios *R*

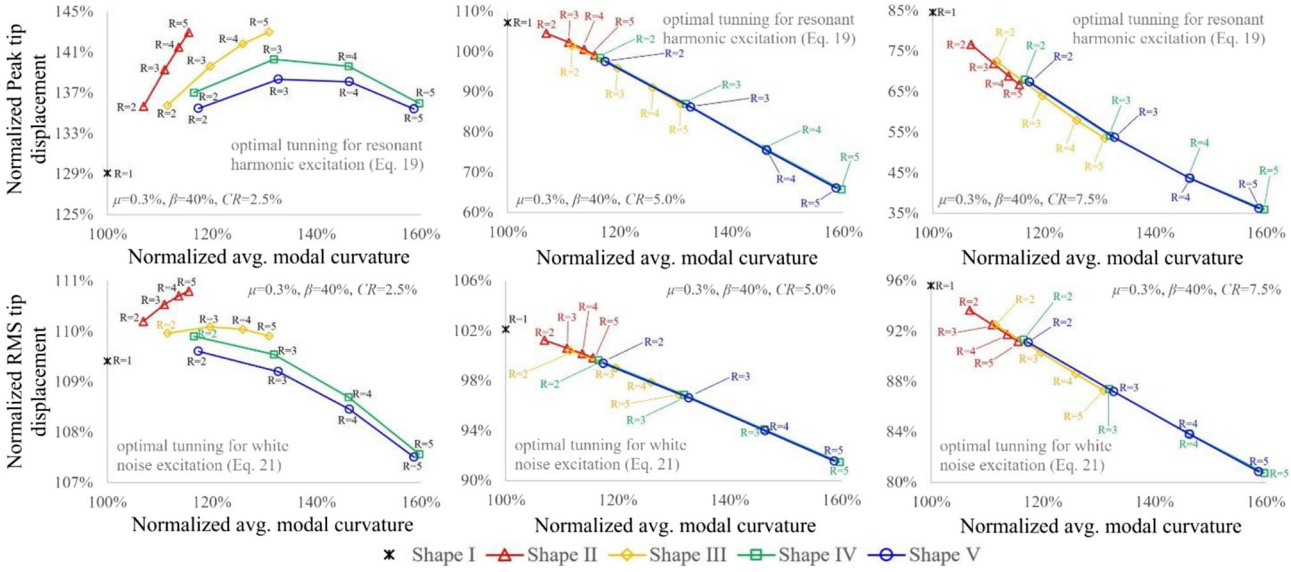

FIGURE 13 Free-end displacement of TMDI-equipped structures under resonant harmonic (upper row) and white noise excitation (lower row) as function of normalized average modal curvature (Figure 8c) for attached mass $m_{TMDI} = 0.3\% \times m^*_{Avg}$, inertance $b = 0.4 \times m^*_{Avg}$, and various inerter connectivity ratios, *CR*, primary structure shapes, and depth ratios *R*. Values are normalized by the corresponding displacement of optimal TMD-equipped structures

5.3 | Influence of depth profile (primary structure shaping) to TMDI stroke and control forces

Having quantified the influence of primary structure shaping on the performance of TMDI-equipped structures in terms of free-end displacement, it is herein deemed essential to gauge the influence of the same on the attached mass

stroke (relative displacement to the free-end displacement), the damping force, and the inerter force. This is because these three quantities are important to the practical design of TMDI-equipped structures. Specifically, TMDI stroke demands relate to the required clearance in housing the attached mass to avoid collisions as well as to the cost of the damping device.[26] Further, the magnitude of the damping and the inerter forces also relate to the cost of the devices and may necessitate special design provisions at the connections of the devices to the primary structure to safely accommodate locally the exerted forces.[31]

The upper row of panels in Figure 14 furnishes bar plots of RMS stroke values σ_{stroke} in Equation (17) for the same structures considered in the upper row of panels in Figures 10 and 11, normalized by the corresponding RMS stroke of optimal TMDs. These data confirm that, irrespective of the primary structure shape, the inclusion of the inerter to the TMD reduces dramatically the attached mass stroke (by more than 90% for all structures considered) as has been reported in several previous studies.[31,33] Nevertheless, it is seen that this relative reduction does not depend significantly on the variation of the primary structure shape due to different depth profile and/or depth ratio. However, the reduction of the RMS stroke with respect to the TMDI stroke for uniform primary structure with $CR = 2.5\%$ depends appreciably on the primary structure shape with more than 40% further reduction observed for all the nonuniformly distributed shapes (bottom row of panels in Figure 14), while it is insensitive to CR. The reduction trends of RMS stroke with respect to the primary structure shape are consistent with the free-end displacement improvement in Figures 10 and 11 and, therefore, very well correlated with the average modal curvature of the primary structure mode shape in Figure 8c. This observation leads to the practically welcoming conclusion that appropriate primary structure shaping, along the same lines as discussed previously, achieves simultaneous reductions in both free-end displacement and TMDI secondary mass stroke.

Further, Figure 15 reports the RMS inerter force, σ_{fb} (upper row of panels), and damping force, σ_{fc} (bottom row of panels), in Equation (17) for the same structures considered in the first row of panels in Figures 10 and 11, normalized by the corresponding forces developing in the uniform primary structure for $CR = 2.5\%$. For all shapes considered, damping forces are seen to increase appreciably with the depth ratio R for fixed depth profile and CR, whereas the increase in inerter forces is less significant. These trends are further visualized in Figure 16, which plots curves of performance (RMS free-end displacement) versus inerter and damping forces for fixed primary structure shapes and different R values. It is seen that, for $CR \geq 5.0\%$, a positive correlation exists between the depth ratio R and the control forces

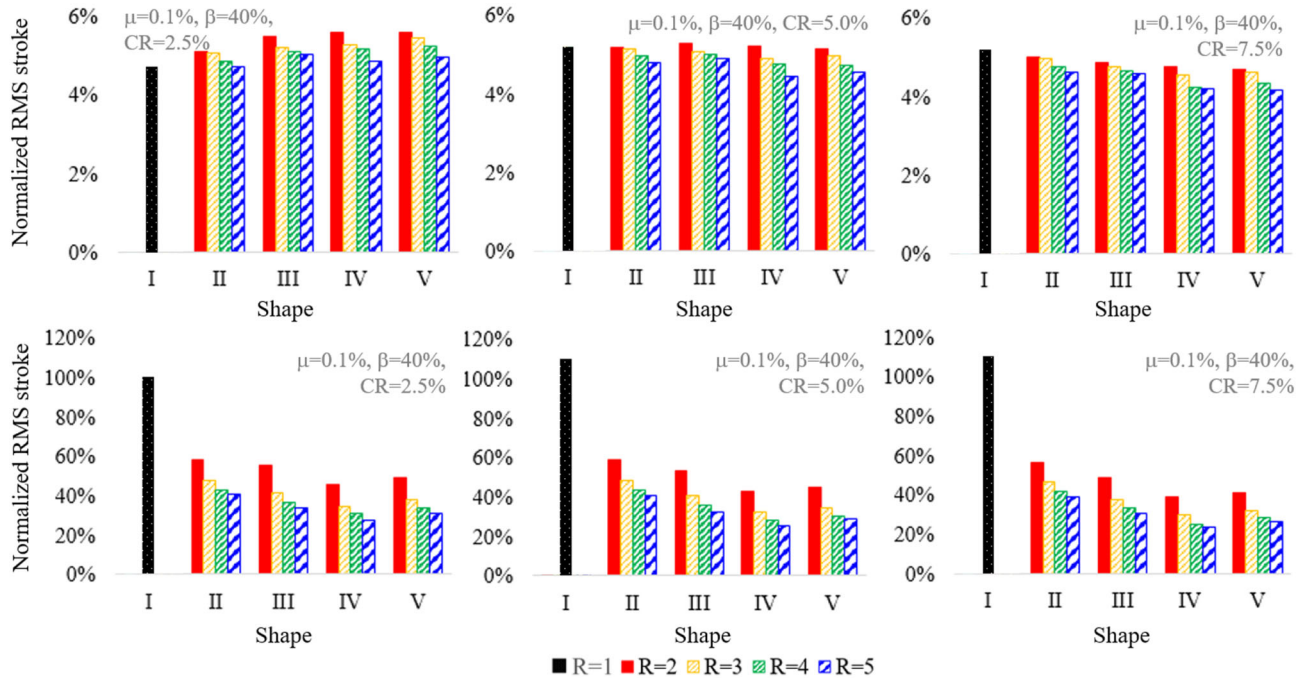

FIGURE 14 RMS TMDI attached mass stroke for TMDI-equipped structures under white noise excitation for attached mass $m_{TMDI} = 0.1\% \times m^*_{Avg}$, inertance $b = 0.4 \times m^*_{Avg}$, and various inerter connectivity ratios, CR, primary structure shapes, and depth ratios R. In the upper row of panels, values are normalized by the corresponding stroke of TMD-equipped structures, and in the bottom row of panels, values are normalized by the stroke of TMDI uniform-shaped structure with $CR = 2.5\%$

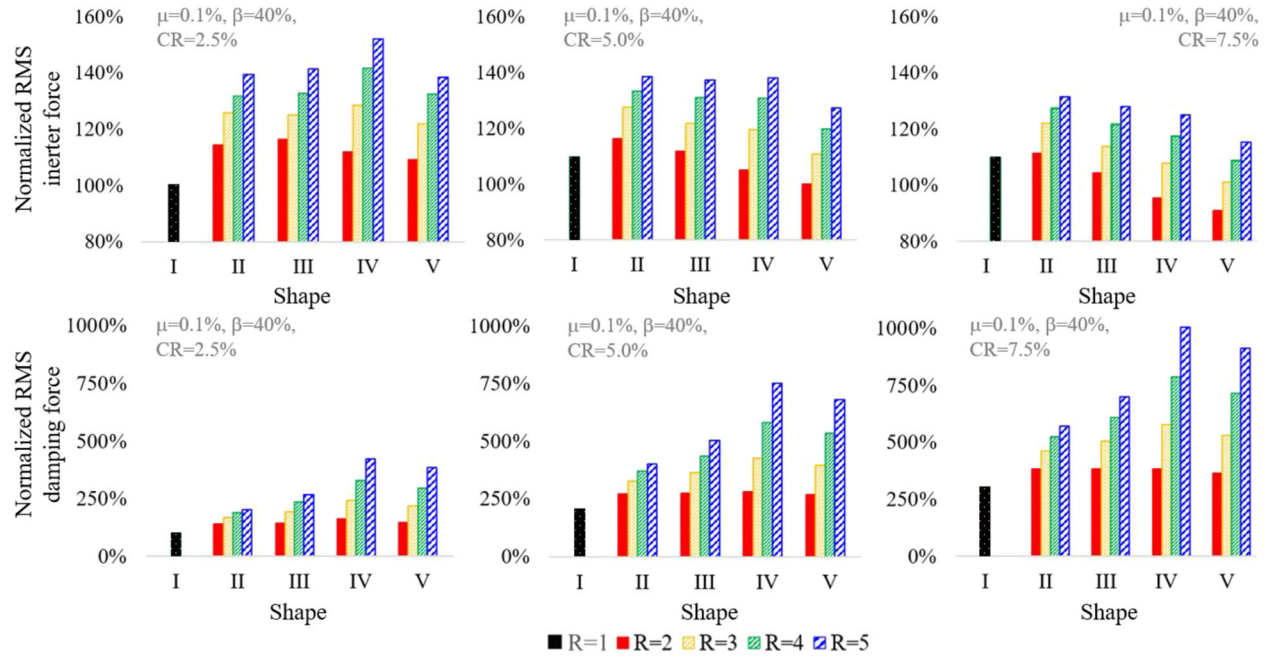

FIGURE 15 RMS inerter resisting force (upper row of panels) and damping force (bottom row of panels) for attached mass, $m_{TMDI} = 0.1\% \times m^*_{Avg}$, inertance $b = 0.4 \times m^*_{Avg}$, and various inerter connectivity ratios, CR, primary structure shapes, and depth ratios R normalized by the corresponding values of optimal TMDI for the uniform primary structure with the inerter connectivity ratio, $CR = 2.5\%$

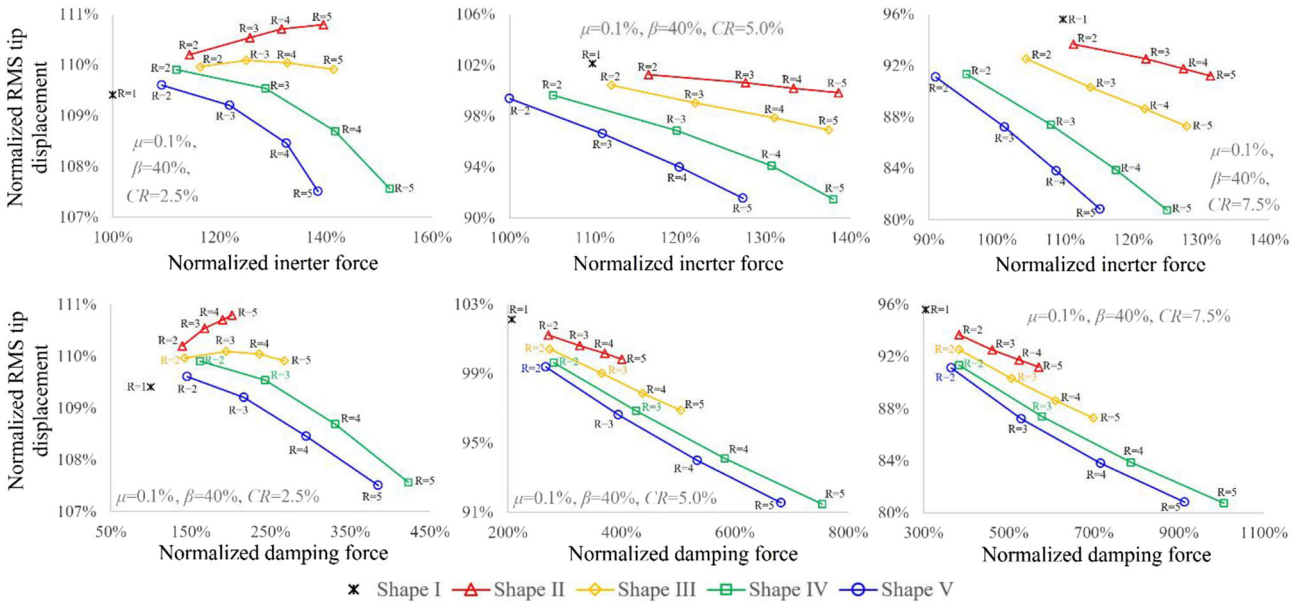

FIGURE 16 RMS free-end displacement versus RMS inerter force (upper row of panels) and damping force (bottom row of panels) for attached mass, $m_{TMDI} = 0.1\% \times m^*_{Avg}$, inertance $b = 0.4 \times m^*_{Avg}$, and various inerter connectivity ratios, CR, primary structure shapes, and depth ratios R. All quantities are normalized by the corresponding values of optimal TMDI for the uniform primary structure ($R = 1$) with $CR = 2.5\%$

within an optimal TMDI design setting. More importantly, structural performance improves almost linearly with the control forces as R increases with higher rate of improvement as the depth profile evolves from "II" towards "V." From a structural design viewpoint, the significance of the above trend is that higher control forces need to be accommodated by the primary structure in case of leveraging R for improved structural performance.

Meanwhile, for the cases that TMDI outperforms TMD ($CR = 5\%$ and 7.5%), it is seen that the inerter force reduces as the depth profile varies from type "II" to type "V" for fixed R (first row of panels in Figure 15). In this respect, judicial selection of depth profile rather than increase of the depth ratio may be preferable for improving structural performance in applications where the magnitude of the inerter force acting at height χ to the structure is critical in design as can be appreciated by examining the first row of panels in Figure 16. Similarly, the magnitude of the damping force is influenced significantly from the depth profile and the depth ratio, as evidenced by the second row of panels in Figure 15. For $CR = 5\%$ and 7.5%, damping force increases as structural performance improves and as depth profile changes from type "II" to type "IV" for fixed R. However, damping forces reduce slightly when going from shape "VI" to "V" for fixed R, while the structural performance remains almost the same as seen in Figure 16.

Collectively, the previous observations and data in Figures 15 and 16 suggest that TMDI damping and inerter control force demands might be contained through judicial shaping of primary structure. This is an important practical consideration since the up-front cost of dampers and inerter devices is well related to the force they need to be designed for.

6 | CONCLUDING REMARKS

The significance of the geometric shape of cantilevered primary structures to the motion control efficacy of the TMDI under resonant harmonic as well as white noise excitations has been herein established. This was achieved through an innovative parametric study involving a wide range of tapered beam-like primary structures with different continuously varying flexural rigidity, $EI(x)$, and mass, $m(x)$, properties but same total weight equipped with TMDIs optimally tuned for resonant harmonic and for white noise excitation. Optimal TMDI tuning and structural performance assessment was expedited through a novel simplified 2-DOF dynamic model in which the primary structure is represented by a generalized SDOF system to accounts for its flexural rigidity and mass distribution as well as its fundamental vibration mode and the location that the inerter connects to the primary structure (CR). The accuracy of the simplified model for TMDI tuning and performance assessment has been numerically verified vis-à-vis detailed FE modeling of primary structures. Structural performance of TMDI-equipped primary structures with different shapes was expressed in terms of peak and RMS free-end displacement for harmonic and white noise excitation, respectively. Further, RMS values of TMDI stroke, inerter force, and damping force were also presented.

Numerical data demonstrated that TMDI motion control efficiency improves monotonically with increasing inertance and CR (distance of inerter connection to the primary structure from the free end) irrespective of the primary structure shape at a reduced rate with best performance always achieved for grounded inerter. More importantly, it was found that improved TMDI performance as well as reduced TMDI stroke are achieved for primary structure shapes in which the ratio $EI(x)/m(x)$ reduces faster with height rendering the upper part of the primary structure more flexible compared to its base. The beneficial effect of such geometric primary structure shaping was attributed to an increase in the convexity of the fundamental vibration mode of the primary structure measured through the averaged modal curvature over height. This was showcased by demonstrating excellent correlation between structural performance improvement and increase of the average modal curvature. In this respect, the herein reported numerical results establish that shaping the uncontrolled primary structure for faster reduction of $EI(x)/m(x)$ is beneficial from a performance-oriented structural design viewpoint as it relaxes requirements for attached mass, leading to more lightweight absorbers and/or reduces requirements of CR, which allows for the inerter to be connected closer to the free end of the primary structure. The former is important as it leads to more lightweight absorbers, the latter is important as it extends the applicability of TMDI to structures where connecting the inerter away from the free end is practically challenging/prohibitive. Furthermore, it was also found that the primary structure shape influences significantly the TMDI inerter and damping control forces exerted to the primary structure and demonstrated that the magnitude of these forces may be reduced through judicial shaping of the primary structure without compromising structural performance.

As a closing note, the fact that the TMDI motion control potential is heavily dependent on the primary structure elastic and mass properties and, ultimately, on the global modal shape of the uncontrolled structure suggests that tailored application-dependent structural design may be key for improved performance of TMDI-equipped structures to dynamic excitations, besides optimal TMDI tuning and inerter connectivity (CR). In this regard, it is envisioned that the numerical data furnished in this study will serve as a useful first stepping stone towards future research endeavors combining optimal device tuning with structural design for ever-more resilient structures to dynamic excitations.

ORCID

Agathoklis Giaralis https://orcid.org/0000-0002-2952-1171

REFERENCES

1. Cabeza L, Barreneche C, Miro L, Morera J, Bartoli E, Fernandez A. Low carbon and low embodied energy materials in buildings: a review. *Renew Sust Energ Rev*. 2013;23:536-542.
2. Huang M. *High-Rise Buildings under Multi-Hazard Environment*. Singapore: Springer Nature; 2017.
3. Christopoulos C, Filiatrault A. *Principles of Passive Supplemental Damping and Seismic Isolation*. Pavia, Italy: IUSS Press; 2006.
4. Li QS, Zhi LH, Tuan AY, Kao CS, Su SC, Wu CF. Dynamic behavior of Taipei 101 tower: field measurement and numerical analysis. *J Struct Eng*. 2011;137(1):143-155.
5. Lu XL, Zhang Q, et al. Improving performance of a super tall building using a new eddy current tuned mass damper. *Struct Control Health Monit*. 2017;24:e1882.
6. Brownjohn JMW, Carden EP, Goddard CR, Oudin G. Real-time performance monitoring of tuned mass damper system for a 183 m reinforced concrete chimney. *J Wind Eng Ind Aerodyn*. 2009;98:169-179.
7. Carrato PJ, Santamont K. Tuned mass damper control of cross-wind excitation of a solar tower. *Paper Presented at Structures Congress 2012*; March 29–31, 2012; Chicago, Illinois, U.S.
8. Zhao B, Gao H, Wang Z, Lu Z. Shaking table test on vibration control effects of a monopile offshore wind turbine with a tuned mass damper. *Wind Energy*. 2018;21(12):1309-1328.
9. Gaur S, Elias S, Hobbel T, Matsagar VA, Thiele K. Tuned mass dampers in wind response control of wind turbine with soil-structure interaction. *Soil Dyn Earthq Eng*. 2020;132:106071.
10. Elias S, Matsagar V. Research developments in vibration control of structures using passive tuned mass dampers. *Annu Rev Control*. 2017;44:129-156.
11. Rana R, Soong TT. Parametric study and simplified design of tuned mass dampers. *Eng Struct*. 1998;20(3):193-204.
12. Sun C, Nagarajaiah A, Dick AJ. Family of smart tuned mass dampers with variable frequency under harmonic excitations and ground motions: closed-form evaluation. *Smart Struct Syst*. 2014;13(2):319-341.
13. Angelis D, Perno MS, Reggio A. Dynamic response and optimal design of structures with large mass ratio TMD. *Earthq Eng Struct Dyn*. 2012;41(1):41-60.
14. Tse KT, Kwok KCS, Tamura Y. Performance and cost evaluation of a smart tuned mass damper for suppressing wind-induced lateral-torsional motion of tall structures. *J Struct Eng*. 2012;138(4):514-525.
15. Smith MC. Synthesis of mechanical networks: the inerter. *IEEE Trans Automat Control*. 2002;47(10):1648-1662.
16. Ikago K, Saito K, Inoue N. Seismic control of SDOF structure using tuned viscous mass damper. *Earthq Eng Struct Dyn*. 2012;41(3):453-474.
17. Lazar IF, Neild SA, Wagg DJ. Using an inerter-based device for structural vibration suppression. *Earthq Eng Struct Dyn*. 2014;43(8):1129-1147.
18. Marian L, Giaralis A. Optimal design of a novel tuned mass-damper–inerter (TMDI) passive vibration control configuration for stochastically support-excited structural systems. *Prob Eng Mech*. 2014;38:156-164.
19. Zhang SY, Jiang JZ, Neild S. Optimal configurations for a linear vibration suppression device in a multistorey building. *Struct Control Health Monit*. 2017;24(3):e1887.
20. Li YY, Zhang SY, Jiang JZ, Neild S. Identification of beneficial mass-included inerter-based vibration suppression configurations. *J Frankl Inst*. 2019;356(14):7836-7854.
21. Taflanidis AA, Giaralis A, Patsialis D. Multi-objective optimal design of inerter-based vibration absorbers for earthquake protection of multi-storey building structures. *J Frankl Inst*. 2019;356(14):7754-7784.
22. Marian L, Giaralis A. Optimal design of inerter devices combined with TMDs for vibration control of buildings exposed to stochastic seismic excitation. In: *Proceedings of the 11th International Conference on Structural Safety and Reliability, ICOSSAR 2013*; June 16–20, 2013; New York, U.S.
23. Giaralis A, Marian L. Use of inerter devices for weight reduction of tuned mass-dampers for seismic protection of multi-story building: the Tuned Mass-Damper-Inerter (TMDI). In: *Proceedings of the SPIE 9799, Active and Passive Smart Structures and Integrated Systems 2016*; 2016; Las Vegas, Nevada, doi: https://doi.org/10.1117/1112.2219324
24. Pietrosanti D, De Angelis M, Basili M. Optimal design and performance evaluation of systems with Tuned Mass Damper Inerter (TMDI). *Earthq Eng Struct Dyn*. 2017;46(8):1367-1388.
25. Giaralis A, Taflanidis AA. Optimal tuned mass-damper-inerter (TMDI) design for seismically excited MDOF structures with model uncertainties based on reliability criteria. *Struct Control Health Monit*. 2017;25:e2082.
26. Ruiz R, Taflanidis AA, Giaralis A, Lopez-Garcia D. Risk-informed optimization of the tuned mass-damper-inerter (TMDI) for the seismic protection of multi-storey building structures. *Eng Struct*. 2018;177:836-850.
27. De Domenico D, Qiao HS, Wang QH, Zhu ZW, Marano G. Optimal design and seismic performance of Multi-Tuned Mass Damper Inerter (MTMDI) applied to adjacent high-rise buildings. *Struct Design Tall Spec Build*. 2020;29:e1781.
28. Kaveh A, Farzam MF, Jalali HH. Statistical seismic performance assessment of tuned mass damper inerter. *Struct Control Health Monit*. 2020;27:e2602.

29. De Domenico D, Ricciardi G. An enhanced base isolation system equipped with optimal tuned mass damper inerter (TMDI). *Earthq Eng Struct Dyn*. 2018;47(4):1169-1192.
30. De Angelis M, Giaralis A, Petrini F, Pietrosanti D. Optimal tuning and assessment of inertial dampers with grounded inerter for vibration control of seismically excited base-isolated systems. *Eng Struct*. 2019;196:109250.
31. Giaralis A, Petrini F. Wind-induced vibration mitigation in tall buildings using the tuned mass damper-inerter (TMDI). *J Struct Eng*. 2017;143(9):04017127.
32. Dai J, Xu ZD, Gai PP. Tuned mass-damper-inerter control of wind-induced vibration of flexible structures based on inerter location. *Eng Struct*. 2019;199(15):109585.
33. Petrini F, Giaralis A, Wang Z. Optimal tuned mass-damper-inerter (TMDI) design in wind-excited tall buildings for occupants' comfort serviceability performance and energy harvesting. *Eng Struct*. 2020;204:109904.
34. Sarkar R, Fitzgerald B. Vibration control of spar-type floating offshore wind turbine towers using a tuned mass-damper-inerter. *Struct Control Health Monit*. 2019;27:e2471.
35. Nakaminami S, Kida H, Ikago K, Inoue N. Dynamic testing of a full-scale hydraulic inerter-damper for the seismic protection of civil structures. In: *Proceedings of the 7th International Conference on Advances in Experimental Structural Engineering, ASCE 2017*; September 6–8, 2017; Pavia, Italy.
36. Pietrosanti D, De Angelis M, Giaralis A. Experimental shaking table study of nonlinear SDOF system equipped with tuned mass damper inerter (TMDI) under harmonic excitation. *Int J Mech Sci*. 2020;184:105762.
37. Giaralis A, Taflanidis AA. Reliability-based design of tuned-mass-damper-inerter (TMDI) equipped stochastically support excited structures. In: *Proceedings of the 12th International Conference on Applications of Statistics and Probability in Civil Engineering (ICASP12)*; July 12–15, 2015; Vancouver, Canada
38. Wang Z, Giaralis A. Performance enhancement of TMDI-equipped tall building in wind-induced vibration via top floor softening. *J Struct Eng*. 2020;147(1):04020283. https://doi.org/10.1061/(ASCE)ST.1943-541X.0002838
39. Pietrosanti D, De Angelis M, Basili M. A generalized 2-DOF model for optimal design of MDOF structures controlled by Tuned Mass Damper Inerter (TMDI). *Int J Mech Sci*. 2020;185:105849.
40. Clough RW, Penzien J. *Dynamics of Structures (3rd Edition)*. U.S.: Computers & Structures, Inc.; 1995.
41. Marian L, Giaralis A. The tuned mass-damper-inerter for harmonic vibrations suppression, attached mass reduction, and energy harvesting. *Smart Structures and Systems*. 2017;19(6):665-678.
42. Cacciola P, Tombari A, Giaralis A. An inerter-equipped vibrating barrier for non-invasive motion control of seismically excited structures. *Struct Control Health Monit*. 2020;27(3):e2474.
43. Chopra AK. *Dynamics of Structures: Theory and Applications to Earthquake Engineering (2nd Edition)*. U.S.: Prentice-Hall; 2001.
44. Charles A, Dennis JE Jr. Analysis of generalized pattern searches. *SIAM J Optim*. 2003;13(3):889-903.
45. Li SY, Liu M, Li HX, Hui Y, Chen ZQ. Effects of structural damping on wind induced responses of a 243-meter-high solar tower based on a novel elastic test model. *J Wind Eng Ind Aerodyn*. 2018;172:1-11.

How to cite this article: Wang Z, Giaralis A. Enhanced motion control performance of the tuned mass damper inerter through primary structure shaping. *Struct Control Health Monit*. 2021;e2756. https://doi.org/10.1002/stc.2756